

Shale distribution effects on the joint elastic–electrical properties in reservoir sandstone

Najeeb S. Aladwani^{1,2,3}  | Laurence J. North² | Ismael Himar Falcon-Saurez²  | Angus I. Best²

¹Department of Earth and Environmental Sciences, Faculty of Science, Kuwait University, Kuwait, Kuwait

²National Oceanography Centre, European Way, Southampton, UK

³Ocean & Earth Science, University of Southampton Waterfront Campus, Southampton, UK

Correspondence

Najeeb S. Aladwani, Department of Earth and Environmental Sciences, Faculty of Science, Kuwait University, P.O. Box 5969, Safat 13060, Kuwait.

Email: Najeeb.aladwani@ku.edu.kw

Abstract

We investigated the effect of shale distribution on the joint elastic wave and electrical properties of shaly reservoir sandstones using a dataset of laboratory measurements on 75 brine-saturated (35 g/L salinity) rock samples (63 samples from the literature, 12 newly measured samples). All the data were collected using the ultrasonic (700 kHz) pulse-echo measurement technique for P- and S-wave velocities (V_p , V_s), attenuations (Q_p^{-1} , Q_s^{-1}), and a four-electrode method for resistivity under elevated hydrostatic confining pressures between 10 and 50 MPa (pore fluid pressure 5 MPa). The distribution of volumetric shale content was classified by comparing the calculated dry P-wave modulus to the modified Upper Hashin–Shtrikman bound for quartz and air mixtures, assuming pore-filling shale. This scheme in particular allowed us to distinguish between pore-filling and load-bearing shale distributions according to idealized definitions, which provides new insight into the joint ultrasonic properties and resistivity behaviour for shaly sandstones. In resistivity–velocity space, the resistivity of load-bearing shale increases with increasing velocity which form a more distinct trend with steeper gradient compared to those for partial pore-filling shale and clean sandstones. Moreover, the pore-filling shale trend straddles the clean sandstone trend and meets the load-bearing shale trend between 100 and 150 apparent formation factors. In resistivity–attenuation space, the highest attenuations exist when the volumetric shale content is close to the frame porosity (for Q_p^{-1} in particular), at the transition between pore-filling and load-bearing shales. The results will inform the development of improved rock physics models to aid reservoir characterization from geophysical remote sensing, particularly for joint seismic and controlled source electromagnetic surveys.

KEYWORDS

joint elastic–electrical properties, petrophysical properties, pressure effects, reservoir sandstones

INTRODUCTION

Understanding the influence of shale distribution on the joint elastic and electrical properties of reservoir sandstones, and pressure dependence, is of great importance to hydrocarbon exploration, reservoir monitoring and characterization. It is

well known that the presence of assemblages of clay mineral particles in a sandstone, often with their own porosity (i.e. shale), can influence both remotely sensed geophysical properties, such as seismic velocity and electrical resistivity, and reservoir properties, such as porosity and permeability (Han et al., 1986; Worthington, 1982). Clay distribution effects

This is an open access article under the terms of the [Creative Commons Attribution](https://creativecommons.org/licenses/by/4.0/) License, which permits use, distribution and reproduction in any medium, provided the original work is properly cited.

© 2023 The Authors. *Geophysical Prospecting* published by John Wiley & Sons Ltd on behalf of European Association of Geoscientists & Engineers.



in sand–clay mixtures, and by analogy in shaly sandstones, are also well appreciated. Marion et al. (1992) showed how seismic velocity is controlled by shale content and distribution in the continuum from clean sand, through shaly sands (i.e. pore-filling shale) and sandy shales (i.e. load-bearing shale), to shale. Revil and Glover (1998) showed similar control of shale content and shale distribution in sands on permeability linked to electrical properties. However, there have been few observational studies of the joint properties of shaly sandstones and the effect of shale content and distribution. This knowledge is needed to validate theoretical models that could be used for joint inversion and interpretation of co-located seismic and electromagnetic survey data.

Carrara et al. (1999) were among the first to measure laboratory joint elastic–electrical properties on sandstone samples. Their focus was to test an electro-seismic model to obtain fluid saturation and porosity; hence, they did not present any systematic relationships between seismic velocity and electrical resistivity. Several authors (Sheng & Callegari, 1984; Salem, 2001; Hacikoylu et al., 2006) used well-logging data to investigate the joint elastic and electrical properties of reservoir rocks. Others used electrical well-logging data for hydrocarbon exploration (Aladwani, 2021, 2022a, 2022b; Aladwani et al., 2023). However, well-log results must be interpreted with caution because of spatial averaging effects for different rock properties and unknown parameters, compared with data collected on small rock samples in the laboratory where rock parameters can be better constrained.

To date, the most systematic and comprehensive laboratory study of joint elastic–electrical properties of shaly sandstones was reported by Han et al. (2011a, 2011c, 2015). They measured the ultrasonic compressional (P -) and shear (S -) wave velocity and attenuation (denoted V_p , V_s , Q_p^{-1} and Q_s^{-1} respectively), and electrical resistivity (ρ), of 63 shaly sandstone samples under effective pressures (i.e. the difference between confining and pore fluid pressures) from 8 to 60 MPa. They observed a systematic influence of clay content on velocity–resistivity relations in particular (Han et al., 2011b), well described by an effective medium model (Han et al., 2011c), and on their pressure dependencies (Han et al., 2011a). Some systematic trends in resistivity–attenuation space were seen, but they were more uncertain.

Recent studies based on joint elastic–electrical properties have demonstrated a considerable reduction in rock resistivity caused by the clay minerals (Carcione et al., 2003; Lee, 2011; Carcione et al., 2012; Peng et al., 2018). Cilli and Chapman (2020) examined the effects of porosity on resistivity and elastic moduli using laboratory measurements on carbonate samples and a power–law relationship between porosity and pore aspect ratio. Pang et al. (2021) created an electrical model and suggested a dual-porosity clay parallel network, and to simulate the elastic properties, they also suggested differential effective medium equations and the Hashin–Shtrikman equations. Then, Pang et al. (2021)

calculated the rock parameters based on saturation, clay content, total porosity and microcrack porosity using these two models. Additionally, a 3D elastic–electrical template was constructed using Poisson's ratio, resistivity and acoustic impedance. Zhang et al. (2022) studied the pore geometrical characteristics of tight sandstones and proposed a multiphase reformulated differential effective-medium model that uses the same pores or fractures with various aspect ratios and volume fractions as the unified pore geometry for both electrical and elastic modelling. The pore structure and mineral make-up of tight-oil rocks are complicated, with a significant percentage of clay (Lu et al., 2019; Gao et al., 2022). Pang et al. (2022) analysed the heterogeneity of tight-oil reservoir rocks from cores by using X-ray diffraction and casting thin sections, to determine the rock mineralogy and pore structure. The impacts of pores, microcracks and mineralogy on the elastic–electrical properties were then investigated using ultrasonic and resistivity studies under various confining pressures. Pang et al. (2021) created acoustic and electrical models based on effective-medium theories, the Cole–Cole and triple-porosity equations. Then, a 3D rock-physical template was constructed and calibrated using the well-log data and core samples (Pang et al., 2021).

Here, we seek insight into the role of shale distribution, in addition to shale content, on the joint properties by applying a quantitative shale classification scheme to the existing Han et al. data, as well as adding new laboratory measurements to validate and extend the previous study. The results both confirm original observations of Han et al. and also point to distinct effects of pore-filling and load-bearing shales on shaly sandstone joint properties.

JOINT SEISMIC AND ELECTRICAL MEASUREMENTS

Sample selection and preparation

A suite of 12 new shaly sandstone samples was chosen carefully to expand the Han et al. dataset. The samples were selected from a repository of several hundred rock samples that were measured previously in the laboratory ultrasonic pulse-echo system (Marks, 1994; Sharp, 1995). These samples came with petrophysical analysis results, including porosity, permeability and clay content, as well as ultrasonic velocity and attenuation that were used to select the best samples for this study. This was achieved by cross-plotting velocity, porosity and permeability for the Han et al. data, and the repository core data, to see where the repository core data could fill in or extend the clay content range of the Han et al. data. The chosen repository core samples are listed in Tables A1 and B1 in the appendices together with their previously measured petrophysical and ultrasound properties, with published sources indicated.

All samples were prepared according to standard procedures described in McCann and Sothcott (1992) and Han et al. (2011b). The samples were cored as 5 cm diameter cylindrical plugs, cut to a length of 2 cm with the two end faces ground flat and parallel to within ± 0.01 mm. The samples were placed into an oven to be dried for 3 days at a temperature of 40°C to conserve clay minerals as far as possible (temperatures above 60°C will destroy clays). The cleaned and dried samples were weighed, their dimensions measured and then they were saturated in 35 g/L brine at an elevated pressure of 7 MPa for 3 days. The saturated samples were then held in a tank filled with the same brine before being transferred into the high-pressure rig for ultrasonic and electrical measurements.

The geophysical parameters P- and S-wave velocity and attenuation, and electrical resistivity, of each sample, were measured in quick succession at each effective pressure of 50, 40, 26, 15 and 8 MPa (the pore fluid pressure was maintained at 5 MPa); the pressure was allowed to equilibrate for 30 min before commencing measurements. The laboratory temperature was maintained at $19 \pm 1^\circ\text{C}$ and relative humidity at $50\% \pm 1\%$.

Joint ultrasound and electrical resistivity tomography RIG

The ultrasonic pulse-echo method (Winkler & Plona, 1982; McCann & Sothcott, 1992) was used to measure P- and S-wave velocities (V_p , V_s) and attenuations (Q_p^{-1} , Q_s^{-1}) at frequencies between 400 and 800 kHz. We used a dual P/S wave transducer giving velocity and attenuation coefficient measurement accuracies of $\pm 0.3\%$ and ± 0.2 dB/cm, respectively (Best, 1992). The high-pressure rig and sample assembly were adapted for resistivity tomography measurements according to North et al. (2013). See Figure 1.

The rubber sleeve surrounding the sample contained 16 stainless steel electrodes in tetrapolar configuration, radially distributed in two rings around the sample. The electrodes allowed current injection and boundary voltage probing in various permutations, giving a resistivity measurement error under typical operating conditions of $\leq 0.1\%$ at frequencies 1–500 Hz, for a sample electrical resistivity range of 1–100 Ω m.

SHALE CLASSIFICATION ANALYSIS

Here, we adapt the method described by Sørensen and Fabricius (2015) for the Han et al. data at the highest pressure of 60 MPa. The results of Han et al. (2011b) demonstrated that the pressure dependence of velocity, attenuation and resistivity are minimal at this high pressure and can be taken as representative of the intact

lithology with negligible stress-release microcrack-related effects.

Sørensen and Fabricius (2015) were able to delineate between four types of so-called clay distribution in a set of sandstones by comparing volumetric shale fraction to grain framework porosity obtained using the method of Gal et al. (1998). Here, “shale” is taken to mean solid clay mineral assemblages, including any associated microporosity and bound water; “clay” refers to the solid clay minerals only (without bound water). They defined the first group as clean sandstone with less than 2% shale measured by image analysis (thin section points counting), and the second group as sandstone with dispersed shale below the critical shale fraction, that is when the shale fraction is less than the sand grain frame porosity. The third group was for sandstone with shale at the critical shale fraction. The fourth group followed the Marion et al. (1992) idea of load-bearing shale, when shale volume exceeds the sand grain frame porosity. This classification depends on the modified upper Hashin–Shtrikman (MUHS) bound (Mavko & Mukerji, 1998; Gal et al., 1999) that connects the theoretical frame porosity to the elastic frame moduli of the sandstone. The majority of the shale was assumed to be authigenic and pore-filling (Sørensen & Fabricius, 2015).

Some factors led us to modify the approach adopted by Sørensen and Fabricius (2015). First, although shale fraction data from image analysis were available to Sørensen and Fabricius (2015), the Han et al. dataset had clay mineral content only from whole rock X-ray diffraction (XRD). Moreover, Sørensen and Fabricius (2015) made the assumption that the measured porosity (obtained by the helium porosimeter method) included the shale fraction porosity, including any bound water. This assumption is open to question because the helium porosimeter measures the effective porosity (i.e. the ratio of interconnected void spaces to the bulk volume), and the degree to which the fine shale pores could be penetrated by the helium gas is not known. Hence, Sørensen and Fabricius (2015) assumed that the difference between the theoretical framework porosity and the measured porosity gives the clay volume (without bound water), whereas, in our analysis, we assume that the difference between the framework porosity and the measured porosity gives the volumetric shale fraction (including any bound water). Sørensen and Fabricius (2015) assumed that the theoretical line (MUHS trend for air and quartz) represents clay, whereas, in nature, shale always comes with bound water and clay (minerals without bound water); so in our approach, the theoretical line in Figure 3 represents volumetric shale fraction, and the application scope is to widen the model to become applicable in natural reservoir shaly sandstone.

Hence, our “shale distribution” classification scheme shown in Figure 2 follows the Sørensen and Fabricius (2015) way of grouping the sandstones; only we use the difference between the theoretical frame porosity and the measured effective porosity from Figure 3 to calculate the shale fraction

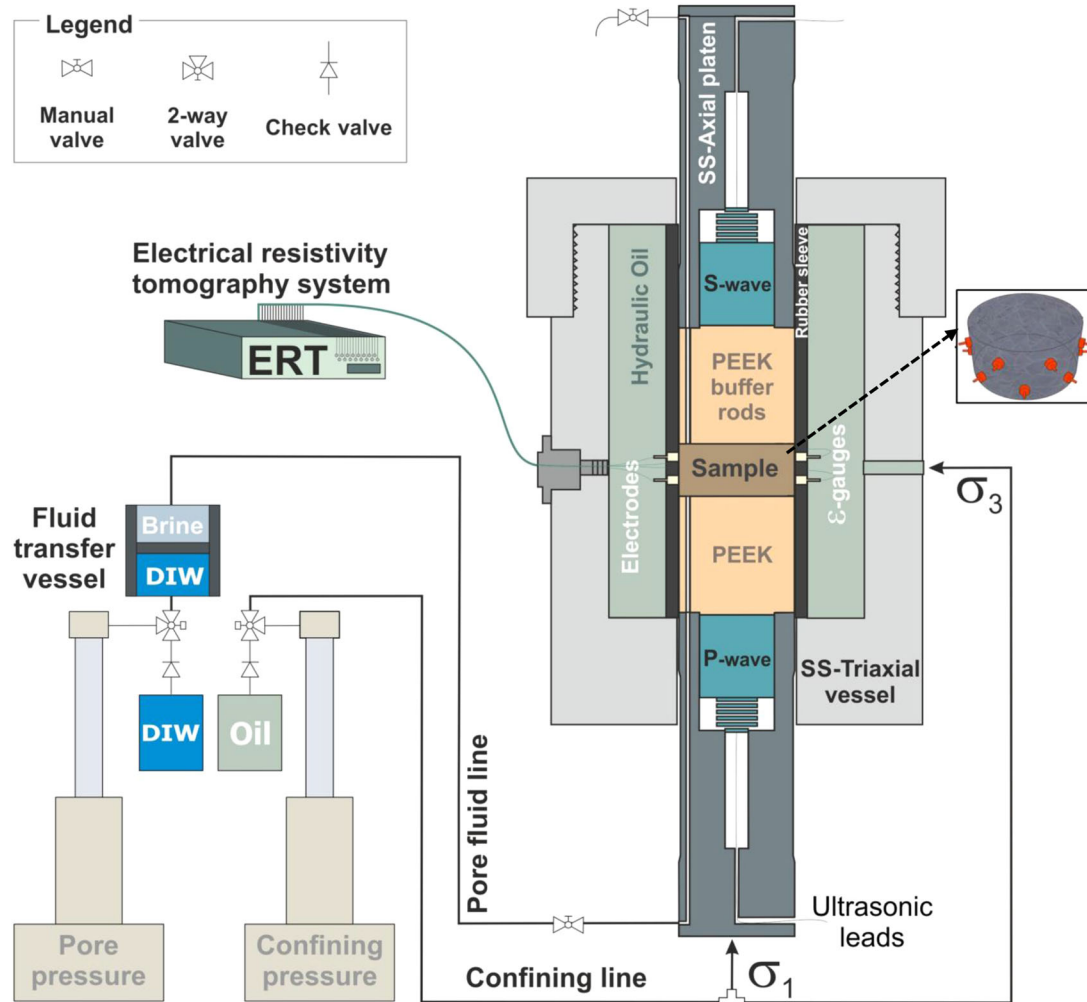


FIGURE 1 Schematic diagram of the experimental set-up, also showing the arrangement of electrodes around the rock sample. Scales are approximate (sample width is 5 cm). ERT, electrical resistivity tomography. *Source:* After Falcon-Suarez et al. (2017) and North et al. (2013).

(see Equation 8). Then, we used the XRD-derived clay content (i.e. volume fraction of solid minerals only, excluding bound water and shale porosity), not shale content, to calculate the shale porosity (including bound water) (see Equation 9). Clean sandstones with less than 2% shale volume fraction are denoted as clean sandstones (Group 1). Group 2 comprises partially pore-filling shale with more than 2% shale volume fraction, and less than 90% of the frame porosity; this last percentage was chosen arbitrarily in an attempt to account for the shale porosity effect, valid for assumed shale porosity and bound water of 20%. Group 3 comprises homogeneous pore-filling shale (i.e. the shale fills the entire frame porosity); we chose an arbitrary interval between 90% and 110% of the frame porosity for this group. Group 4 is denoted load-bearing shale when the volumetric shale fraction is more than the upper limit of Group 3. Therefore, there is sufficient volumetric shale present for sand grains to be supported by a shale–grain framework (sandy shale).

The MUHS curve describes how the elastic moduli of clean sandstones evolve from deposition through compaction

and cementation. It is not a rigorous bound on the elastic properties of clean sand, although sandstone moduli are almost always observed to lie on or below the MUHS curve (Mavko et al., 2009). Further, terms like “stiff pore shapes” and “soft pore shapes” are used usually to describe the data with respect to the MUHS curve.

The few data that were above the MUHS trend have significant amounts of minerals with higher elastic moduli than quartz such as carbonates or feldspars and belong to clean sandstones, so we assume the measured porosity is the frame porosity as there was a negligible shale fraction or none at all.

The frame porosity was calculated from the dry compressional wave modulus M_{dry} for each sample at 60 MPa (Mavko et al., 2009). In Figure 3, the solid line represents the MUHS trend for air and quartz, which basically represents rocks with quartz minerals in framework and pores filled with air without shale or any other minerals, so the pores here are frame porosity. The samples with shale in pore space and in the framework lie below the solid line. The frame porosity can be computed for each shaly sandstone sample (see Figure 3 small

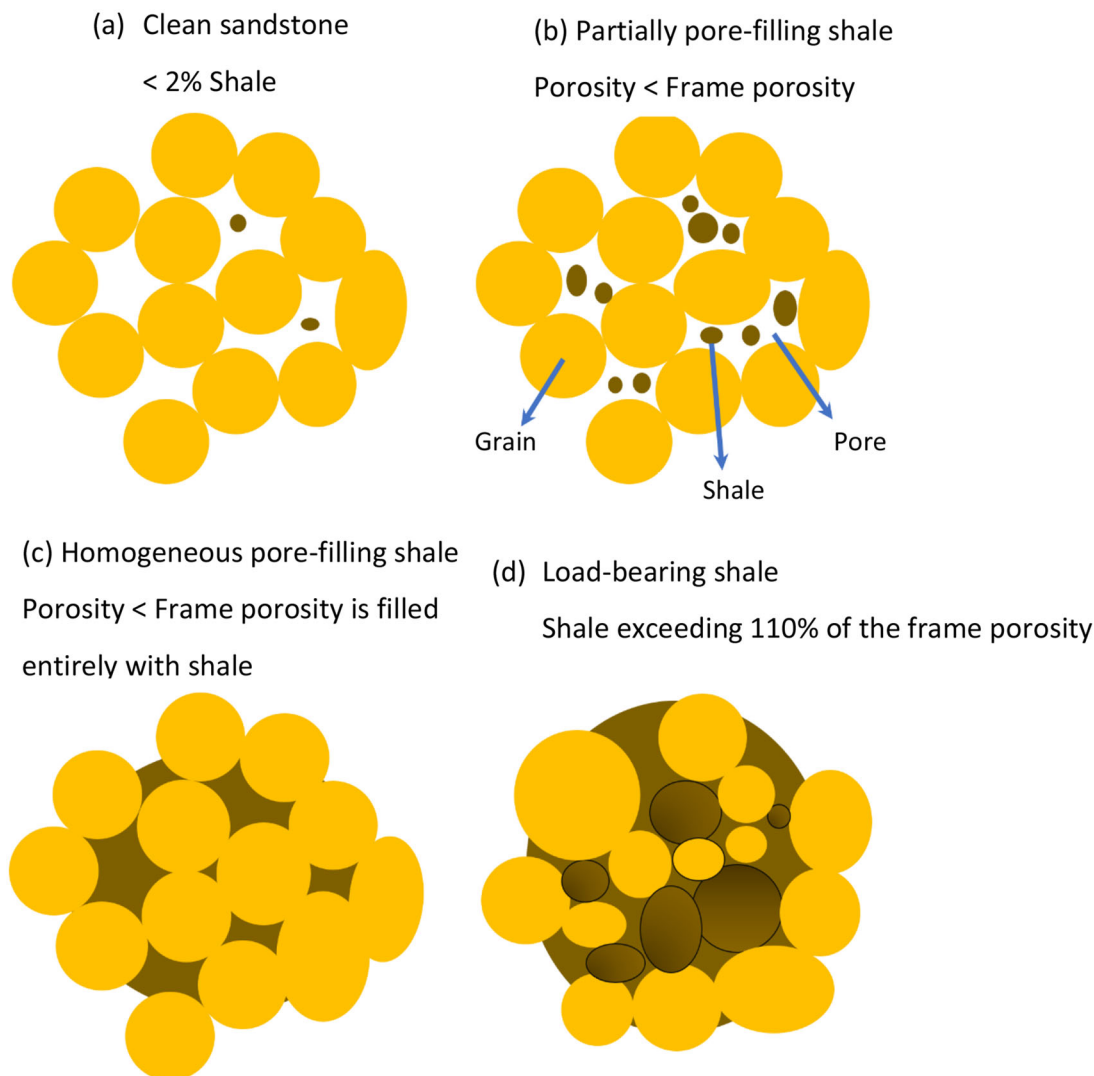


FIGURE 2 The shale distribution classification scheme used in this study. a) represents clean sandstone with less than 2% shale, b) A rock with partial pore-filling shale in which the frame porosity is more than porosity, c) a rock with Homogenous pore-filling shale in which the frame porosity is filled with shale, d) a rock with Load-bearing shale is when the shale exceeding 110% of the frame porosity and some of the shales is part of the framework of the rock. *Source:* Adapted from Sorensen and Fabricius (2015).

graph, frame porosity fit) by fitting the samples to the solid line (MUHS). Then, frame porosity can be obtained. However, samples above the solid line contain shale less than 2%, so they belong to Group 1.

As the sandstones were measured under brine saturation conditions, the dry bulk modulus K_{dry} was obtained using the following Gassmann fluid substitution (Gassmann, 1951):

$$K_{\text{dry}} = \frac{K_{\text{sat}} \left(\phi \frac{K_o}{K_{f1}} + 1 - \phi \right) - K_o}{\phi \frac{K_o}{K_{f1}} + \frac{K_{\text{sat}}}{K_o} - 1 - \phi}, \quad (1)$$

where ϕ is porosity, K_o is the mineral bulk modulus, K_{f1} is the pore fluid bulk modulus and K_{sat} is the saturated bulk modulus. The dry compressional modulus is then calculated from

$$M_{\text{dry}} = K_{\text{dry}} + \frac{4}{3} G, \quad (2)$$

where G is the dry frame shear modulus, equal to the measured saturated rock shear modulus according to Gassmann's theory.

Shale classification and group delineation

Figure 3 shows dry compressional modulus and porosity, colour-coded by clay content for all the 75 sandstones. The sandstone samples were colour-coded by clay content just to show that samples with clay content lie significantly below the solid line. The differences between the measured

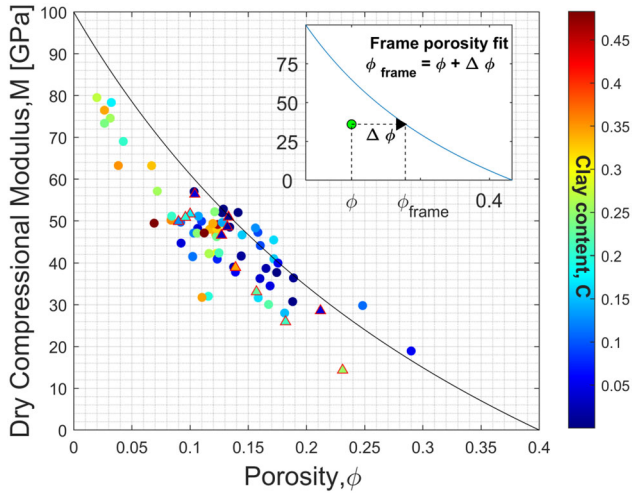


FIGURE 3 Shale classification diagram according to porosity and dry compressional modulus for the 63 shaly sandstone samples of Han et al (2011a, 2011b, 2011c) in circle and 12 newly measured sandstone samples in triangle. The solid line represents the modified upper Hashin–Shtrikman trend (MUHS) for air and quartz. *Source:* Adapted from the method of Sørensen and Fabricius (2015).

porosity and framework porosity are shale volume fraction and from here on we will use shale volume fraction in our analysis. The solid line is the MUHS bound for a critical porosity equal to 0.4 and a pure quartz compressional mineral modulus $M_0 = 100$ GPa (Koga et al., 1958). The MUHS bound represents the diagenetic trend for clean sandstone as the rock becomes progressively quartz cemented, with the quartz cement occupying the pore space and reducing porosity from the critical porosity. The MUHS curve is computed using the following equations:

$$z = \frac{G_s}{6} \frac{9K_s + 8G_s}{K_s + 2G_s}, \quad (3)$$

$$G_{\text{Dry}} = \left[\frac{\phi/\phi_b}{G_b + z} + \frac{1 - \phi/\phi_b}{G_s + z} \right]^{-1} - z, \quad (4)$$

$$K_{\text{Dry}} = \left[\frac{\phi/\phi_b}{K_b + \frac{4}{3}G_s} + \frac{1 - \phi/\phi_b}{K_s + \frac{4}{3}G_s} \right]^{-1} - \frac{4}{3}G_s, \quad (5)$$

$$M_{\text{dry}} = K_{\text{dry}} + \frac{4}{3}G, \quad (6)$$

where K_s is quartz grain bulk modulus (GPa), G_s is quartz grain shear modulus (GPa), K_b is quartz grain bulk modulus at the critical porosity (GPa), G_b is quartz grain shear modulus at the critical porosity, ϕ_b is the critical porosity, M_{sat} is the saturated compressional modulus, K_{sat} is the saturated bulk modulus and G is the shear modulus (Dvorkin et al., 1999).

Figure 3 illustrates that sandstone samples with low shale fraction are close to the MUHS trend line, and samples with higher shale fraction lie significantly below the MUSH trend. Thus, the measured rock porosity is lower than the idealized quartz frame porosity due to the presence of shale. Samples above the MUHS line might have minerals that have higher elastic moduli than quartz such as feldspars or carbonates. These samples have negligible shale fraction and fall within the clean sandstone group. We followed the Gal et al. (1999) assumption that the difference in porosity between the idealized frame porosity according to MUHS, ϕ_{frame} , and the measured rock sample value ϕ_e (or effective porosity) gives the shale volume fraction X , in the pore space of the framework according to

$$\phi_{\text{frame}} = \phi_e + X, \quad (7)$$

where X is shale fraction. The framework porosity ϕ_{frame} for each sample in the dataset can be determined by comparing the measured porosity to the MUHS trend as illustrated in the small graph inset in Figure 3.

Further, the volumetric shale fraction X in the pore space of the framework can be determined by

$$X = \phi_{\text{frame}} - \phi_e. \quad (8)$$

The shale porosity $\phi_{\text{sh}} (= V\phi_{\text{sh}}/V_{\text{sh}}$, where V with subscripts ϕ_{sh} and V_{sh} are the volumes of shale porosity and shale, respectively). For partial pore-filling shale and homogenous pore-filling shale, it can be determined from volumetric shale fraction $X (= V_{\text{sh}}/V_{\text{rock}}$, where V_{rock} is the total rock volume) and solid clay fraction $C (= V_{\text{Cl}}/V_{\text{rock}}$, where V_{Cl} is the solid clay mineral volume) from

$$\phi_{\text{sh}} = 1 - (C/X) \quad (9)$$

Then, the shale microporosity (ϕ_{sh}) was determined by Equation (9) where C is solid clay fraction without shale microporosity obtained from XRD, and X is shale fraction calculated from Equation (8). We will use only the shale fraction in the following analysis.

Figure 4 shows framework porosity against volumetric shale fraction. It illustrates the final shale distribution classification for 75 sandstone samples. Clean sandstones in Figure 4 (green triangle) are defined as those that contain less than 2% (the vertical blue line represents 2%) of shale by volume (Group 1). In order to account for the shale porosity effect, Group 2 consists of partially pore-filling shale with more than 2% shale volume fraction and less than 90% of the frame porosity; this last percentage was picked at random and is valid for an assumed shale porosity and bound water of 20% as shown in Figure 4 (pink square). We arbitrarily selected a range between 90% and 110% (the inclined

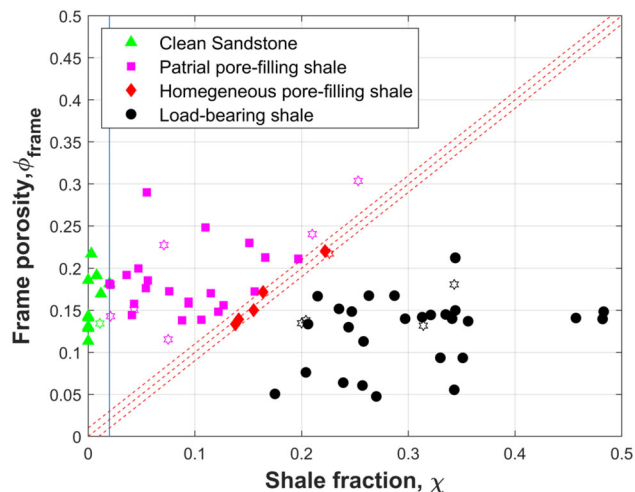


FIGURE 4 Shale classification diagram according to shale fraction χ , and frame porosity for the 63 shaly sandstone samples of Han et al (2011b). Samples with star symbols represent the 12 new samples. The dashed red lines represent 90% and 110% of shale filling the framework porosity. *Source:* Method adapted from Sørensen and Fabricius (2015).

red dashed line in Figure 4) of the frame porosity for Group 3 (red diamond in Figure 4), which consists of homogenous pore-filling shale, to represent this group. When the volumetric shale portion exceeds the top limit of Group 3, it is said to be load-bearing shale, which belongs to Group 4 (black circle in Figure 4). Because of this, therefore, there is enough volumetric shale present for a shale–grain structure to support sand grains (sandy shale). It can be seen that this particular dataset contains a reasonable spread of samples in all four shale classification groups. This allows us to draw some conclusions about the role of shale distribution on the joint elastic–electrical properties.

Figure 5 is a histogram showing the distribution of shale porosity that was obtained from Equation (9). The shale porosity distribution is in general negatively skewed if we exclude the data below 2% shale porosity; they have low shale content and were classified as clean sandstone. The mean value of shale porosity for all samples is 0.63. The mean value for partial pore-filling shale samples is 0.39, and for load-bearing shale, it is 0.78. The shale porosity distribution is consistent with the shale porosity distribution published by Hurst and Nadeau (1995) and Sørensen and Fabricius (2015). The mean value of 0.63 in this study is close to the mean values of 0.59 reported by Sørensen and Fabricius (2015) and $65\% \pm 14\%$ reported by Vernik (1994). Figure 5 shows a maximum shale porosity of around 0.7 for sandstone with pore-filling shale, which is similar to that of Vernik (1994) and also agrees with the maximum shale porosity of about 0.7 of Sørensen and Fabricius (2015).

Figure 6 shows an example of load-bearing and partial pore-filling shales in thin sections to visually validate the

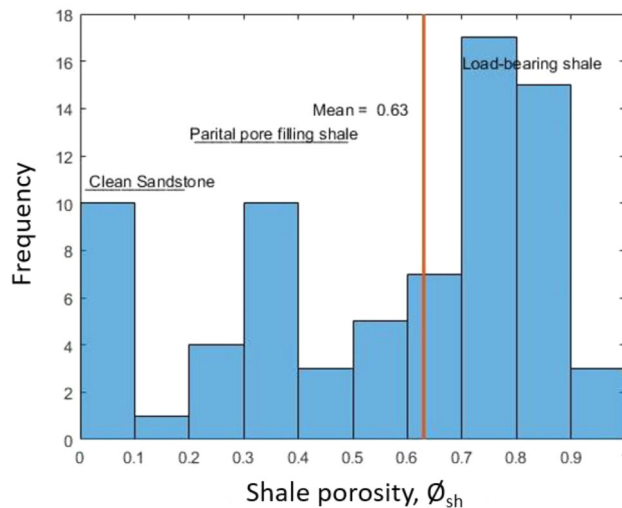


FIGURE 5 Histogram of shale porosity obtained from Equations (9) and (10).

assumption of load-bearing shale in the framework of the rock. In Figure 6a, the shale is insufficient to become part of framework, but shale is clearly part of the framework in Figure 6b. The Group 4 load-bearing shale might be dispersed within the pore space or laminated, as can be seen in Figure 6b.

RESULTS – THE EFFECT OF SHALE DISTRIBUTION ON JOINT ELASTIC–ELECTRICAL PROPERTIES

Velocity–resistivity (apparent formation factor F^*)

Han et al. (2010) were able to draw some conclusions on the joint velocity and resistivity relationship here called the velocity–resistivity relationship for short. Han et al. (2011c) expressed their resistivity results as apparent formation factor F^* , defined as ρ_0/ρ_w , the resistivity of the sample saturated with brine (ρ_0) to the resistivity of the brine (ρ_w), and we will follow that convention here.

Han et al. (2011b) were able to distinguish visually two limbs on the F^* -velocity cross-plots corresponding to clay-rich and clean sandstone trends with some scatter of data points. Here, we produce similar plots for F^*-V_p and F^*-V_s for this extended dataset and use clustering analysis to obtain a statistical estimate of the significance of different groupings of data points (Tan et al., 2005; Chen & Hoversten, 2012).

The K -mean clustering technique is a type of unsupervised training algorithm to treat the observations in data as objects having locations and distances from each other (Liu et al., 2004). The procedure involves choosing k initial centroids,

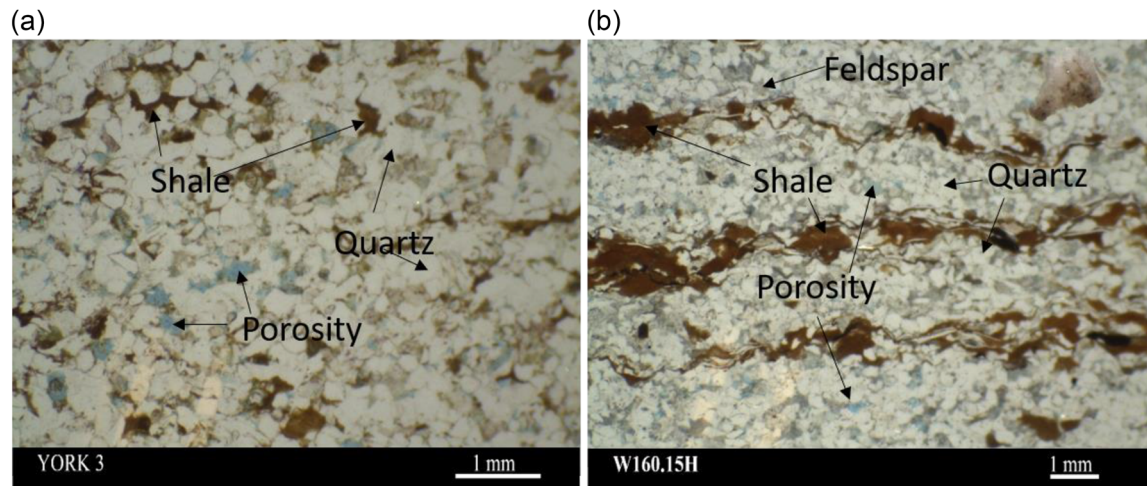


FIGURE 6 Thin section images showing the shale distribution within (a) partial pore-filling shale (York 3) Group 2, and (b) load-bearing shale (W160.15H) Group 4.

where k is some clusters, usually the desired user-specified parameters; here, we tried $k = 2-5$ as shown in Figure 7. K -mean clustering then assigns each data point to its nearest centroid, and each group of data points assigned to a centroid becomes a cluster. The centroid of each cluster is then iteratively refined as new data points are assigned to the cluster. The algorithm finally converges when no further change occurs to the clusters (Chauhan et al., 2016; Lee et al., 2017). Figure 7 shows that the initial visual interpretation of Han et al. of two groups can be reasonably extended to three groups using K -mean clustering with $k = 3$.

In Figure 7, we compare the results of the K -mean clustering algorithm for $k = 3$ to the delineation of shale groups according to our shale classification scheme. Three clustering groups can be seen in Figure 7b: Cluster 3 (red colour) appears as a transition between Cluster 1 (blue) and Cluster 2 (black).

In general, F^* increases with increasing V_p (and V_s in Figure 8) with shale-rich sandstones forming a steeper, separate trend than clean sandstones, as noted by Han et al. (2011b). Furthermore, we can now separate the shale-rich sandstone trend into two more trends, one dominated by homogeneous pore-filling shale and partial pore-filling shale (as indicated by Cluster 3) and the other by load-bearing shale (as indicated by Cluster 2). The partial pore-filling shale trend straddles the clean sandstone and load-bearing shale patterns. However, the load-bearing shale pattern is relatively tightly constrained, and the data points only overlap with a few of the pore-filling shale trend samples. We see similar trends for V_p and V_s in Figure 8 (Aladwani et al., 2016).

Porosity and joint properties

Porosity plays a critical role that affects both elastic and electrical properties of reservoir rocks (Archie, 1942; Han et al.,

1986; Klimentos & McCann, 1990; Best et al., 1994; Han et al., 2011b). Porosity reduces the bulk and shear moduli of the solid framework of the reservoir rock which, in turn, affects the velocity of compressional and shear waves. In general, porosity increases attenuation due to the viscous interaction of pore fluids and solid framework (Biot, 1956; Murphy et al., 1986; Klimentos & McCann, 1990). Moreover, increasing porosity increases the electrical conductivity (decreases the electrical resistivity) when saturated with brine due to an increase in permeability allowing greater diffusion of free ions through the electrolyte (Klimentos & McCann, 1990).

Figure 9 shows cross-plots between apparent formation factor F^* and P- and S-wave velocities, respectively, colour-coded by porosity. In general, apparent formation factor and velocity increase with decreasing porosity as noted by Han et al. (2011b). However, with our new analysis, we can see that there are three behaviours in the cross-plots between apparent formation factor F^* and P- and S-wave velocities, respectively. The first behaviour is the trend in clean sandstone and sandstones with partial pore-filling shale that have apparent formation factors less than 70 and porosity more than 13%. The second behaviour is for sandstones with homogenous pore-filling and the partial pore-filling shales that have apparent formation factors above 70 and porosity around 12%. This trend is above the clean sandstone trend. The third behaviour is the load-bearing shale, showing a steeper trend for porosity less than 12%.

Figure 10 shows cross-plots of F^* versus P- and S-wave attenuations ($F^*-Q_p^{-1}$ and $F^*-Q_s^{-1}$, respectively), colour-coded by porosity. In general, attenuation and porosity increase with F^* up to a value of about $F^* = 100$. The maximum attenuation occurs at porosities between 10% and 15% and then decreases. Low shale content sandstones appear to the left of the attenuation maximum and shale-rich

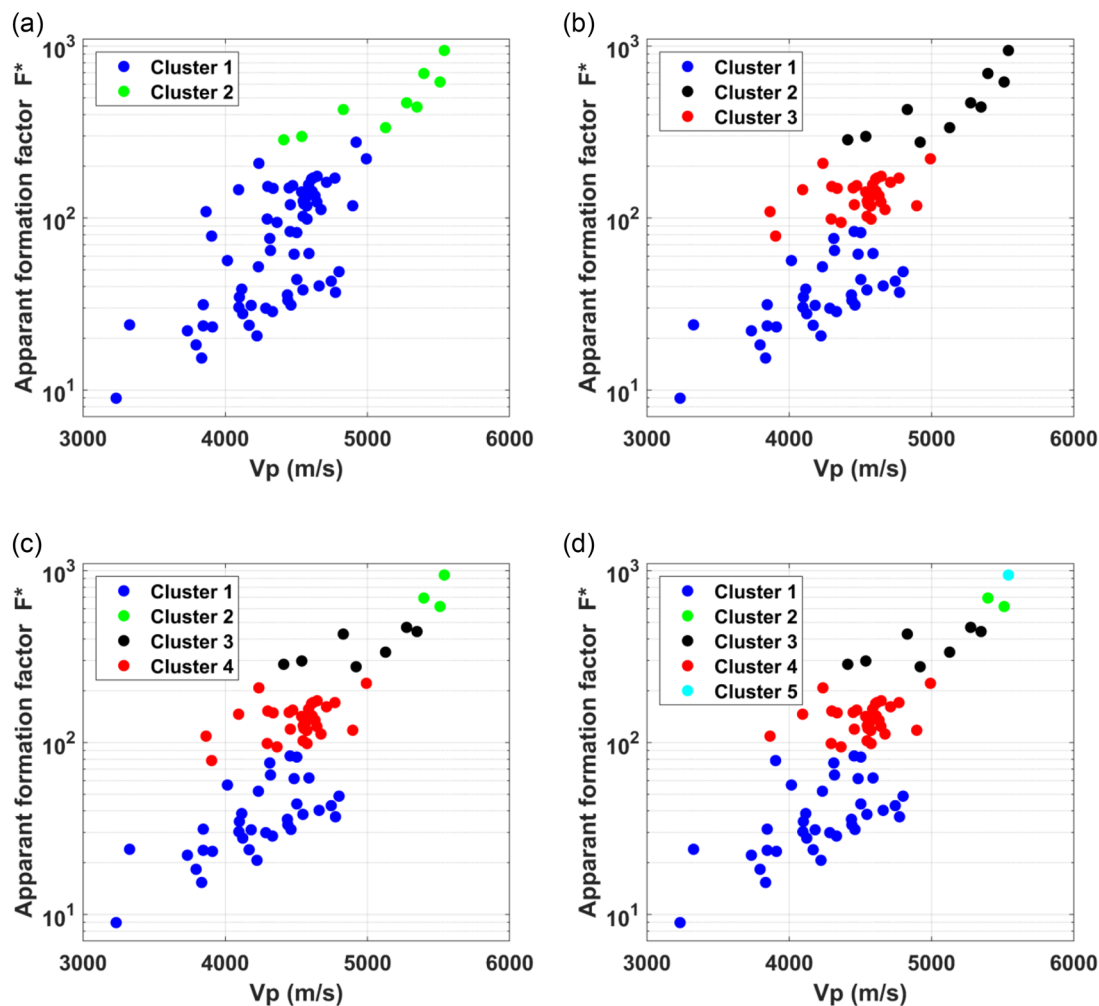


FIGURE 7 Scatter diagram showing P-wave velocity against apparent formation factors colour-coded by *K*-mean clustering methods: (a) $K = 2$, (b) $K = 3$, (c) $K = 4$ and (d) $K = 5$.

sandstones to the right, as noted by Han et al. (2011b). We are now able to determine from our shale classification scheme that (i) the right-hand decreasing trend is dominated by load-bearing shale with porosity less than 10% with the lowest attenuation, and (ii) the left-hand trend is dominated by a mix of clean and partial pore-filling shale sandstones with porosity above 15%, and some overlap between trends. There are similar trends for Q_p^{-1} and Q_s^{-1} , although there is more scatter of low F^* data points for Q_s^{-1} as noted by Han et al. (2011b). In general, P-wave attenuation has the highest values when shale content is close to the frame porosity, at the transition between pore-filling and load-bearing shales.

Overall, the application of the shale classification scheme to the data in Figures 7 and 8 and Figures 9 and 10 shows that shale distribution within sandstones has a significant impact on the joint seismic-resistivity response, and this is related to the relative proportions of shale and sand grains. As can be seen in Figure 9, the trend in clean sandstone and sandstones with partial pore-filling shale, which has apparent formation factors less than 70 and porosity greater than 13%, is the

first behaviour. The second behaviour is seen in sandstones with homogeneous pore filling and shale that partially fills some of the pores and has apparent formation factors above 70 and porosity around 12%. The clean sandstone trend lies underneath this one. The load-bearing shale exhibits the third behaviour, which displays a sharper tendency for porosity less than 12%. Thus, different proportions of shale and sand in pore space or in the framework of the rock exhibit different behaviours (Figure 9). However, the transition between pore-filling and load-bearing shales occurs where P-wave attenuation values are highest when shale content is close to the frame porosity in Figure 10.

In accordance with the present results, previous studies have demonstrated the effect of petrophysical properties such as porosity and clay content on the joint properties. Han et al. (2011b) divided the sandstone samples into two groups, clean sandstone with less than about 10% clay content and clay-rich sandstone with more than about 10% clay content. Han et al. (2011b) concluded that porosity does not control the joint velocity and resistivity properties, despite porosity

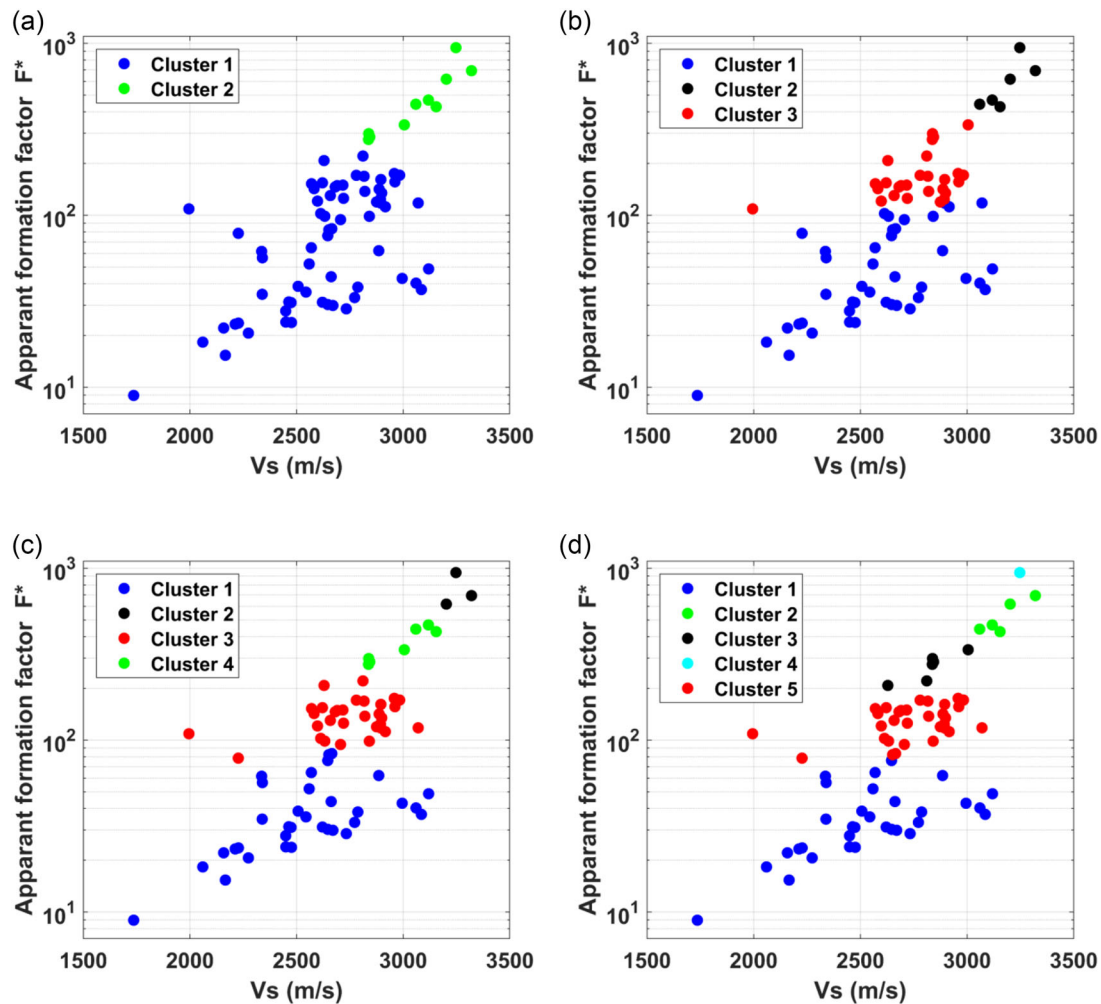


FIGURE 8 Scatter diagram showing S-wave velocity against apparent formation factors colour-coded by K -mean clustering methods: (a) $K = 2$, (b) $K = 3$, (c) $K = 4$ and (d) $K = 5$.

having a strong influence on both elastic and electrical properties independently of each other. Because sandstone samples with similar porosity were found in both groups. However, I apply a statistical analysis (clustering method) and effective medium model (shale classification scheme) to the data and find out that the clustering technique divides the data into three categories (Figure 7b). The clustering techniques suggest further dividing the data into two groups in Han et al. (2011b) to further subdivide the dataset into more than two groups. The use of an effective medium model (shale classification scheme) to the data shows how the pore-filling and load-bearing shales affect joints' elastic–electrical properties. I concluded that the framework of the rock has significant influence on the joint properties whether the framework is sand-born (clean sandstone and partial pore-filling shale) or shale-born (load-bearing shale). In resistivity–velocity space (Figure 9), load-bearing shale forms a distinct trend to Group 1 (clean sandstone) and Group 2 (partial pore-filling shale) and gives rise to decreasing attenuation with increasing appar-

ent formation factor. Moreover, in resistivity–velocity space, pore-filling shale touches the load-bearing shale trend and straddles the clean sandstone trend and gives rise to increasing attenuation with increasing resistivity up to a maximum when shale content is about equal to frame porosity, at the transition between pore-filling and load-bearing shales (Figure 10).

Pressure sensitivity and joint properties

Least-squares regression analysis was used to quantify the effect of shale distribution on the pressure dependence of elastic wave velocity and attenuation, and electrical resistivity, of shale-rich sandstones. Following Han et al (2011a), it is well established from various studies (Eberhart-Phillips et al., 1989; Jones, 1995; Khaksar et al., 1999; Kaselow et al., 2004; Han et al., 2011b) that an equation of the form

$$N = A - Be^{-CP_{\text{diff}}}, \quad (10)$$

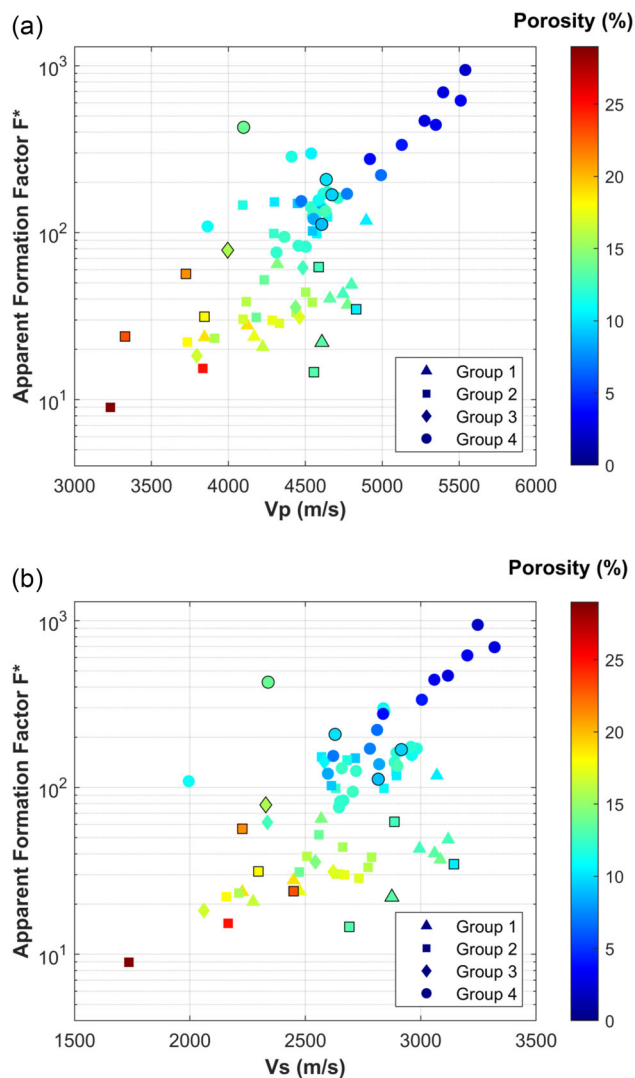


FIGURE 9 Scatter diagram for the Han et al. (2011b) data showing (a) P-wave and (b) S-wave velocities against apparent formation factors colour-coded by porosity at differential pressure 50 MPa. The dark outlined points are new data collected in this study.

can accurately describe the pressure dependence of all five geophysical parameters, that is P- and S-wave velocity (V_p , V_s) and attenuation (Q_p^{-1} , Q_s^{-1}) and electrical resistivity ρ . The variable N corresponds to the geophysical parameters of interest; A , B and C are the best fit regression coefficients, and P_{diff} is the effective pressure. Figure 11 shows the regression curves and data for the four newly measured reservoir rocks, colour-coded according to the shale classification scheme (V_s and Q_s^{-1} results have been omitted as they follow similar trends to those for V_p and Q_p^{-1}). In general, these results agree with Han et al. (2011a), indicating that V_p and ρ increase, and Q_p^{-1} decreases, gradually until the rate of change converges to constant values at higher effective pressures. A possible explanation for pressure-dependent behaviour is the closure of small aspect ratio pores and micro pores (Meglis et al., 1996; Glover et al., 2000). Such low aspect ratio pores and micro

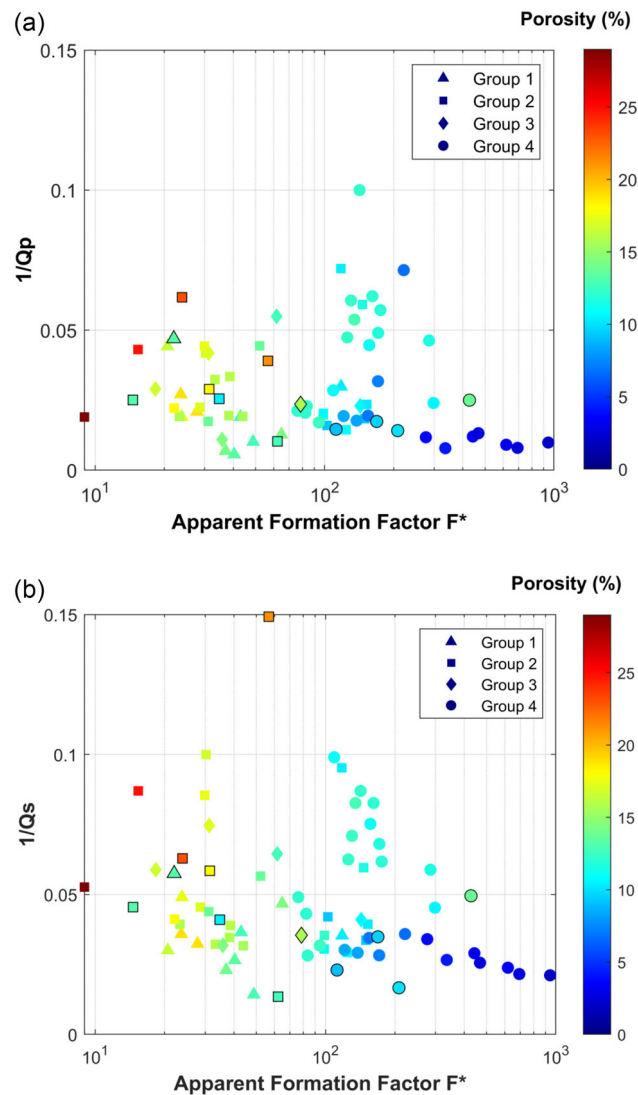


FIGURE 10 Scatter diagram for the Han (2010) data showing (a) P-wave attenuation and (b) S-wave attenuation against apparent formation factors colour-coded by porosity at differential pressure 50 MPa. The dark outlined points are new data collected in this study.

pores could be due to cracks present either within a mineral grain or at grain contacts or might be related to shale minerals with their platy grains and associated microporosity.

A possible explanation for decreases in attenuation with pressure might be that microcrack squirt flow reduces as a result of cracks being closed according to mechanisms explained by Murphy et al. (1986) and Dvorkin et al. (1995). The finite attenuation at higher effective pressure might be explained by background Biot-type losses (Biot, 1956) or might be due to clay-squirt flow (Best & McCann, 1995; Marketos & Best, 2010; Han et al., 2011b). By contrast with V_p and Q_p^{-1} in Figure 11a,b, electrical resistivity in Figure 11c shows systematic increases according to increasing shale content, from clean to partial pore-filling shale, to homogenous pore-filling shale, to load-bearing shale, with the highest

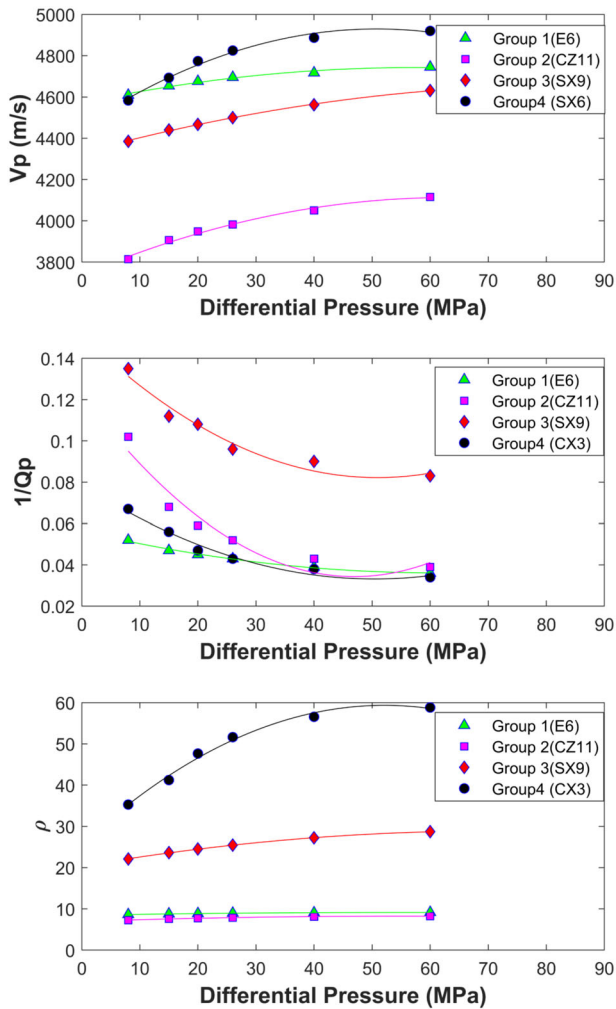


FIGURE 11 Experimental data and regression curves for four newly measured samples showing the dependence on effective pressure of (a) P-wave velocity, (b) P-wave attenuation and (c) electrical resistivity. S-wave velocity and S-wave attenuation show similar trends to those for P-waves. Samples are classified according to shale distribution.

resistivity in the load-bearing shale samples; F^* also increases with pressure according to Equations (3)–(11). A likely explanation for the increase in electrical resistivity with effective pressure is the closure of the narrow conduction pathways at grain contacts. Han et al. (2011b) noted that electrical resistivity is more pressure sensitive in shale-rich sandstones. Our results also show that the load-bearing samples are the most pressure sensitive, followed by those with partial pore-filling shale, then those with homogenous shale, then lastly clean sandstones in a clear succession.

Figure 12 shows the pressure dependence of the joint property $F^* - V_p$ of the four newly measured sandstones, colour-coded according to the shale distribution scheme ($F^* - V_s$ relationships are similar in Figure 12b). The gradients can be seen to increase systematically both as F^* and V_p magni-

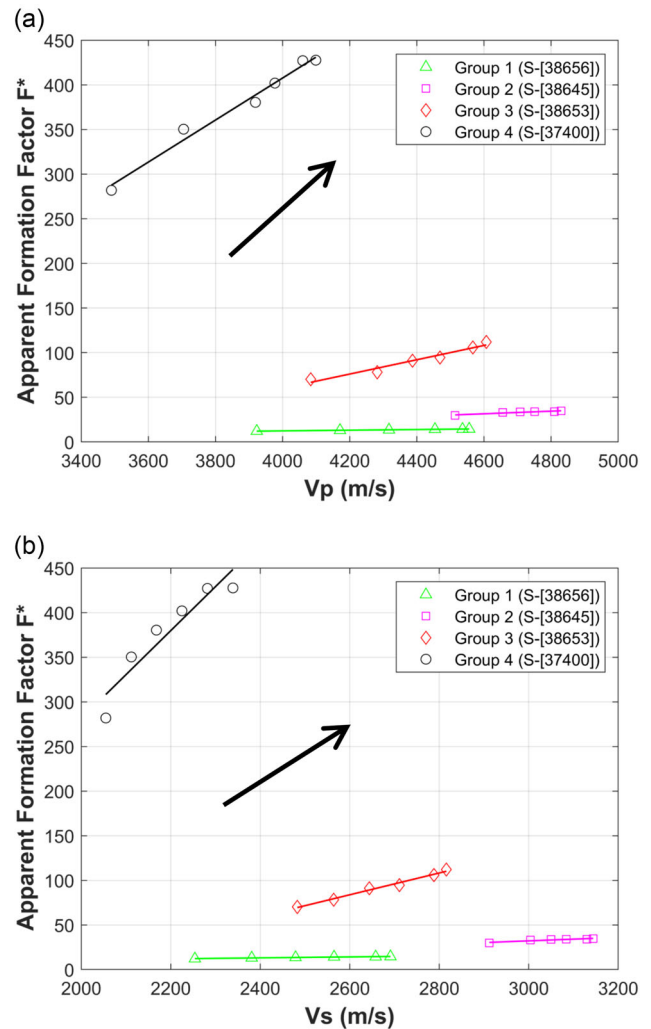


FIGURE 12 Examples of (a) P-wave velocity V_p and (b) S-wave velocity V_s against electrical formation factor F^* for different shale distributions in sandstones, for effective pressures 8–60 MPa (for each sandstone, data points in sequence of 8, 20, 30, 40, 50 and 60 MPa from left to right). Arrows show the direction of increasing differential pressure.

tudes increase, and with increasing shale content from clean sandstone through pore-filling and load-bearing shales.

Linear least-squares regression equations were derived for the joint elastic–electrical data according to

$$\log(F^*) = A V_p + B. \quad (11)$$

The results are shown in Appendices A and B together with regression coefficients R^2 . Figure 11 reveals that there has been an increase in a pressure sensitivity of electrical resistivity in particular (relative to that of V_p and V_s) from partial to homogenous pore-filling shale, to load-bearing shale (which has the highest sensitivity) (Aladwani et al., 2017); previously, Han et al. (2011b) proposed a similar effect for total clay content. Clean sandstone has the lowest resistivity due to

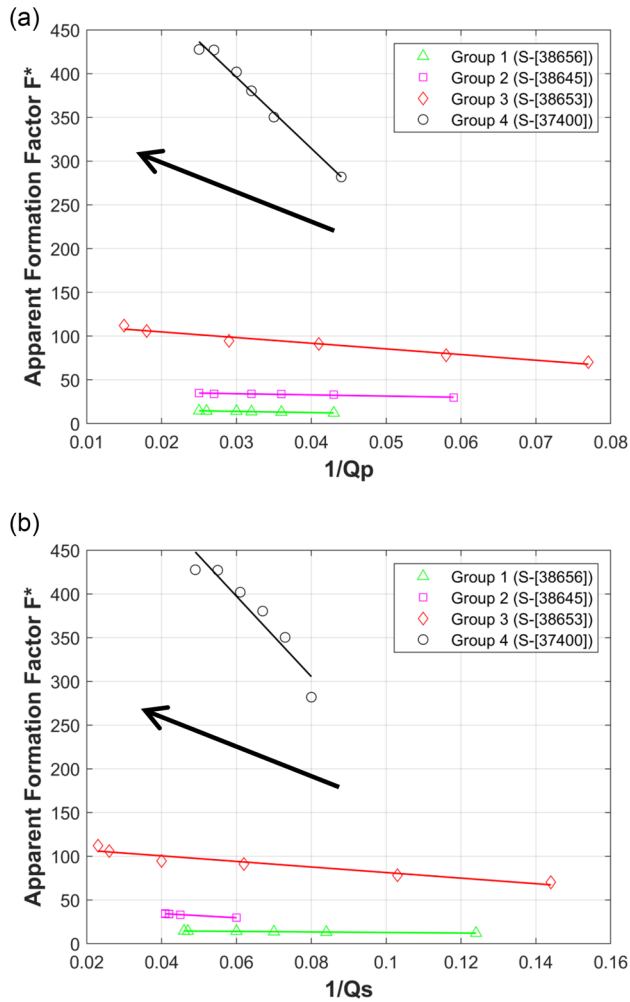


FIGURE 13 Examples of (a) P-wave attenuation $1/Q_p$ and (b) S-wave attenuation $1/Q_s$ against electrical formation factor F^* for different shale distributions in sandstones, for effective pressures 8–60 MPa (for each sandstone, data points in sequence of 8, 20, 30, 40, 50 and 60 MPa from left to right). Arrows show the direction of increasing differential pressure.

the high ionic conduction pathway that move freely in pore space. We see a sharp increase in sensitivity between partial pore-filling and load-bearing shales, indicating different roles in quartz grain framework-dominated porosity versus shale-grain framework-dominated porosity. In the latter, the pores are more susceptible to pressure changes than in the former.

Figure 13 shows the pressure dependence of the joint property (a) $F^*-Q_p^{-1}$ of the four newly measured sandstones, colour-coded according to the shale distribution scheme ($F^*-Q_s^{-1}$ relationships are similar). The gradients can be seen to decrease systematically both as $F^*-Q_p^{-1}$ magnitudes decrease, and with decreasing shale content from clean sandstone through pore-filling and load-bearing shale. However, the load-bearing shale shows steeper decreasing slope than the rest.

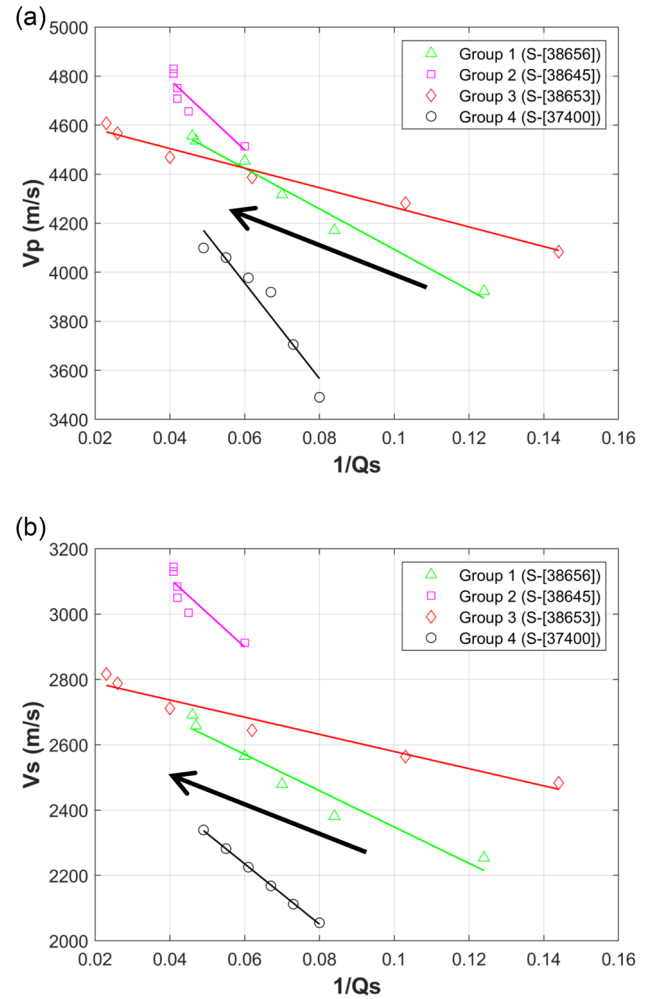


FIGURE 14 Examples of (a) P-wave velocity V_p against P-wave attenuation $1/Q_p$ and (b) S-wave velocity V_s against S-wave attenuation $1/Q_s$ for different shale distributions in sandstones, for effective pressures 8–60 MPa (for each sandstone, data points in sequence of 8, 20, 30, 40, 50 and 60 MPa from left to right). Arrows show the direction of increasing differential pressure.

Apparent formation factor increases with increasing differential pressure, whereas attenuation decreases with increasing differential pressure (Han et al., 2011a). The attenuation with differential pressure data conforms to the results of Jones (1995), Best and Sams (1997) and Han et al. (2011a).

Figure 13 shows the load-bearing shales have the highest apparent formation factor than the rest and have more steeper slope (note $F^*-Q_s^{-1}$ shows similar effect).

Figure 14 shows the pressure dependence of the joint property (a) $V_p-Q_p^{-1}$ of the four newly measured sandstones, colour-coded according to the shale distribution scheme ($V_s-Q_s^{-1}$ relationships are similar in Figure 14b). The clean sandstone and load-bearing shale for $V_p-Q_p^{-1}$, in particular, show a steeper decreasing gradient of velocity with increasing attenuation, whereas partial pore-filling and homogenous pore-filling shales show a gentle

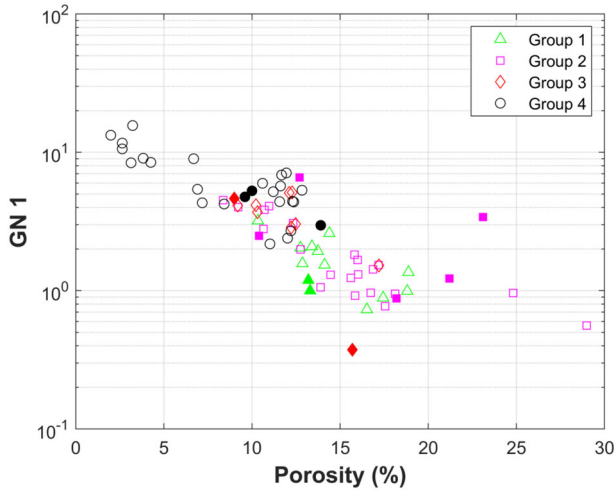


FIGURE 15 Scatter diagram showing the relationship between porosity and the GN1 parameter (pressure sensitivity of the resistivity– V_p curve). GN1 for resistivity– V_s against porosity shows a similar behaviour. The open symbols are (Han et al., 2011a) data, and solid symbols are new measurements from this study.

decreasing gradient of velocity with increasing attenuation (note $F^* - Q_s^{-1}$ shows similar effect).

Effect of shale distribution on seismic and electrical properties

In this section, we reproduce the parameter cross-plots of Han et al. (2011a), but with the new shale distribution classification imposed. Han et al. (2011a) previously indicated only total clay content, not shale distribution. In a similar way to Han (2010), we used the following equations to quantify pressure sensitivity in the form of parameters GN1, GN2 and GN3:

$$GN1 = \frac{(\rho_{60 \text{ MPa}} - \rho_{8 \text{ MPa}}) / \rho_{8 \text{ MPa}}}{V_{p \text{ 60 MPa}} - V_{p \text{ 8 MPa}} / V_{p \text{ 8 MPa}}}, \quad (12)$$

$$GN2 = \frac{(\rho_{60 \text{ MPa}} - \rho_{8 \text{ MPa}}) / \rho_{8 \text{ MPa}}}{(1/Q_{p \text{ 60 MPa}} - 1/Q_{p \text{ 8 MPa}}) / 1/Q_{p \text{ 8 MPa}}}, \quad (13)$$

$$GN3 = \frac{(V_{p \text{ 60 MPa}} - V_{p \text{ 8 MPa}}) / V_{p \text{ 8 MPa}}}{(1/Q_{p \text{ 60 MPa}} - 1/Q_{p \text{ 8 MPa}}) / 1/Q_{p \text{ 8 MPa}}}. \quad (14)$$

Note that Equations (12)–(14) express the pressure sensitivities in a normalized form, to aid comparisons of magnitudes of GN1, GN2 and GN3; Han (2010) used different, non-normalized definitions for G1, G2 and G3 reported therein. Figure 15 shows GN1, the normalized pressure sensitivity of

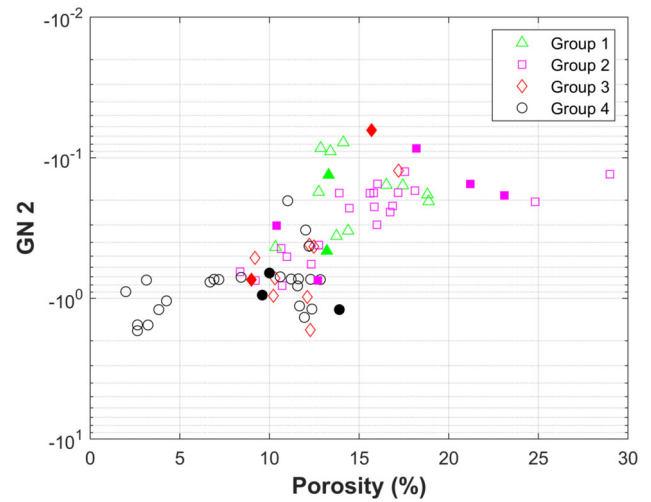


FIGURE 16 Scatter diagram showing the relationship between porosity and the GN2 parameter (pressure sensitivity of the resistivity– Q_p^{-1} curves). GN2 for resistivity– Q_s^{-1} against porosity shows a similar behaviour. The open symbols (Han et al., 2011a) data, and solid symbols are new measurements from this study.

the relationship between resistivity ρ and P-wave velocity V_p against porosity for the 75 shale-rich sandstones. In general, GN1 decreases with porosity, similar to observations of Han et al. (2011a) for G1; the scatter around this trend is approximately constant. Despite the transition from load-bearing shale samples to pore-filling shale with increasing porosity, the pressure sensitivity of the electrical resistivity – V_p relation remains broadly constant on this log–linear scale. Hence, there is an exponential decrease in pressure sensitivity with porosity that is independent of shale distribution.

Figure 16 shows GN2, the normalized pressure sensitivity of the relationship between resistivity ρ and P-wave attenuation Q_p^{-1} against porosity for the 75 shale-rich sandstones. Generally, GN2 decreases in magnitude (becomes less negative and approaches zero) with increasing porosity, from sandy shale (load-bearing shale) to shaly sandstones (i.e. with heterogeneous and critical pore-filling shale) and clean sandstones. However, there is a cluster of points for both sandy shales and shaly sandstones at about 10%–13% porosity that shows a much wider range of GN2 values than at lower and higher porosities. At this stage, it is unclear whether this observation is significant.

Figure 17 shows GN2 against attenuation for the 75 shaly sandstones. Han et al. (2011a) noted the same scatter of data points with no apparent correlation. However, when applying the shale classification scheme, we can see that pore-filling shale has generally lower pressure sensitivity (i.e. less negative and smaller magnitude) than load-bearing shale. This suggests that, in a load-bearing sandstone, the dominant pressure sensitivity is dominated by resistivity. Moreover,

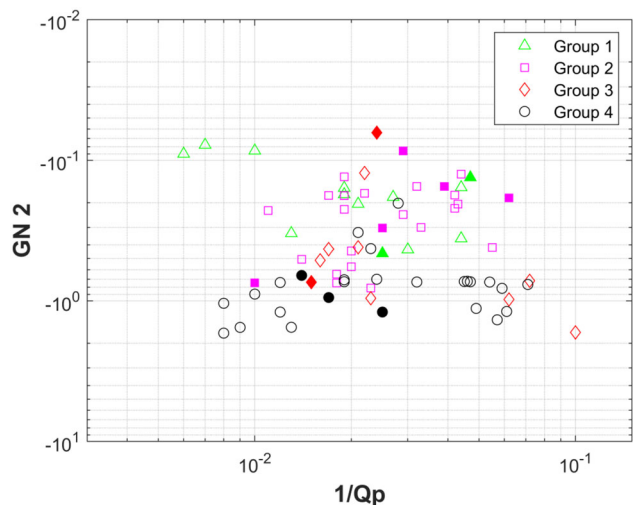


FIGURE 17 Scatter diagram showing the relationship between GN2 and Q_p^{-1} . A similar trend is seen for GN2 against Q_s^{-1} . The open symbols are (Han et al., 2011a) data, and solid symbols are new measurements.

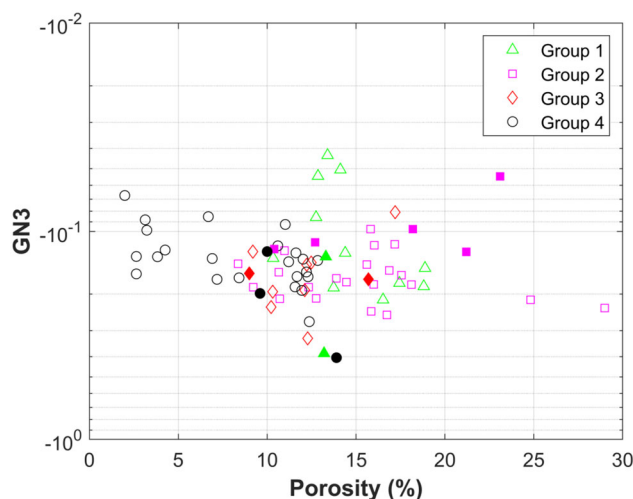


FIGURE 18 Scatter diagram showing the relationship between porosity and the GN3 parameter (pressure sensitivity of the $V_p-Q_p^{-1}$ curves). GN3 for $V_p-Q_s^{-1}$ against porosity shows a similar behaviour. The open symbols are (Han et al., 2011a) data, and solid symbols are new measurements.

load-bearing shales seem to follow a curving trend with G2 increasing to a maximum around $Q_p^{-1} = 0.03$ and then decreasing for higher Q_p^{-1} values. It is difficult to discern trends for the shaly can clean sandstones as the scatter is high.

Figure 18 shows GN3, the normalized pressure sensitivity of the relation between P-wave velocity V_p and attenuation Q_p^{-1} against porosity. It can be seen that the GN3 magnitude decreases with increasing porosity (i.e. becomes more negative). In general, this trend is linear except for values between about 10%–13% porosity as noticed by Han et al. (2011a) for G3.

This indicates higher pressure sensitivity for elastic properties (GN3) around the critical porosity, whether load-bearing or pore-filling shale. This suggests some connection with the degree of disorganization (heterogeneity) of the mineral grains in the sandstone. The shale classification scheme adopted here is idealized, but around the critical porosity, we would expect possibly some load-bearing shales and some pore-filling shales distributed in patches throughout the sandstone.

The shale distribution classification scheme provides more insight in the relationship between quartz grain-born framework, shale–grain-born and the pressure sensitivity of the rock. Figure 15 shows GN1 against porosity, load-bearing shale is dominated at lower porosity, whereas at higher porosity, the clean and partial pore-filling shales are dominated. This suggests the significant impact of the shale–grain-born framework and of low aspect ratio pore in lower porosity, whereas quartz grain-born framework and high aspect ratio pore in high porosity. The relationship between the normalized velocity–attenuation (GN3) and porosity is complete because of the attenuation sensitivity to macropores in the clean sandstone (Group 1), partial pore filling (Group 2) and microporosity in homogenous pore-filling (Group 3) and load-bearing shales (Group 4) in Figure 18 because elastic velocity is not sensitive to various pore types. The GN3 covers less than two orders of magnitude, whereas GN1 and GN2 cover about three orders of magnitude. Therefore, the shrinkage of micro pores in homogenous pore-filling and load-bearing and macroporosity in clean sandstone and partial pore-filling due to changing of differential pressure is much larger in resistivity than attenuation.

CONCLUSIONS

This is the first time a shale classification scheme was applied on a comprehensive joint elastic–electrical dataset of 75 sandstones samples with a broad range of petrophysical properties and as a function of effective pressure from 8 to 60 MPa. We were able to investigate how load-bearing and pore-filling shales affect joint elastic–electrical properties. The following original conclusion can be drawn from the results:

1. Statistical cluster analysis in resistivity–velocity space on a semi-logarithmic scale provided evidence for at least three groups that coincide with the three substantial groups of a shale classification scheme (clean sandstones, shaly sandstones and sandy shales). Sandy shales (load-bearing shale, Cluster 3) have the highest values of F^* and V_p and show the tightest grouping and steepest trend of all three clusters. Cluster 2 is a clean sandstone and partial pore-filling shale. The pore-filling shale trend straddles

the clean sandstone trend and touches the load-bearing shale trend in resistivity–velocity space (Cluster 1). All the three clusterings were approximately linearly correlated in resistivity–velocity space.

2. Partial pore-filling shale seems to give rise to increasing attenuation with increasing electrical resistivity up to a maximum when shale content is about equal to frame porosity. However, load-bearing shale seems to give rise to decreasing attenuation with increasing resistivity. Overall, the highest attenuations occur when the volumetric shale content is close to the frame porosity (for Q_p^{-1} in particular), at the transition between pore-filling and load-bearing shales.
3. Changes of parameters measured, such as compressional and shear wave velocity, attenuation and electrical resistivity with effective pressures, when applying shale classification scheme on the dataset, seems to agree with Equation (8) which is $N = A - Be^{-C P_{diff}}$, where N is petrophysical parameter of interest, A , B and C are the best fit coefficients and P_{diff} is the effective pressure.
4. We demonstrated how load-bearing and partial pore-filling shales affect the relationships between resistivity and velocity, resistivity and attenuation and velocity and attenuation with effective pressure. Resistivity has a high degree of sensitivity to pressure in sandstones with load-bearing shale compared to those with pore-filling shale.
5. We showed that elastic properties (V_p and Q_p^{-1} shown here, but the same result applies for S-waves), at around the critical porosity, seem to be more sensitive to effective pressure when there is a high degree of heterogeneity among the sandstone mineral grains. On the contrary, when dominated by load-bearing or by pore-filling shale, the grains might have a more homogeneously distributed shale, and the pressure sensitivity follows a more predictable trend when compared to, for example porosity.
6. Pressure sensitivity is greatest for load-bearing shale when resistivity is involved in the cross-plot.
7. The pressure sensitivity of ultrasonic velocity and attenuation cross-plot is dominated by the quartz grain framework and microcracks in shaly sandstones, and by load-bearing shale in sandy shales.

The results give further guidance for the development of joint property rock physics models, needed for better geophysical property inversions and improved reservoir characterization. These are needed to aid with interpreting geopressure changes in the reservoir and overburden shaly sandstones.

DATA AVAILABILITY STATEMENT

The data that support the findings of this study are available in Appendix A.

ORCID

Najeeb S. Aladwani  <https://orcid.org/0000-0003-2081-3124>

Ismael Himar Falcon-Saurez  <https://orcid.org/0000-0001-8576-5165>

REFERENCES

- Aladwani, N. (2022a) Qualitative and quantitative analysis of the crustal basement structure using gravity anomaly maps of Kuwait. *Kuwait Journal of Science*, 49, 1–16.
- Aladwani, N., Best, A., North, L. & Minshull, T. (2016) Clay distribution effects on the joint elastic-electrical properties of shaly sandstones. In: *78th EAGE conference and exhibition 2016*. ISBN 2214-4609.
- Aladwani, N., North, L. & Best, A. (2017) Pressure effects on the joint elastic-electrical properties of shaly sandstones based on clay distribution. In: *79th EAGE conference and exhibition 2017*. ISBN 2214-4609.
- Aladwani, N.S. (2021) Assessment of petroleum system of Arabian–Iranian Basin in Kuwait. *All Earth*, 33, 108–123.
- Aladwani, N.S. (2022b) Evaluation of the hydrocarbon source rock and the reservoir characterization of the Minagish Formation using wireline logs. *Heliyon*, 8, e09797.
- Aladwani, N.S., Alenezi, A. & Diab, A. (2023) Investigation of the Cretaceous total petroleum system using wireline logs, core, and geochemical data in Bahrah Field, Northern Basin, Kuwait. *Journal of Petroleum Exploration and Production Technology*, 13(1), 381–406.
- Archie, G.E. (1942) The electrical resistivity log as an aid in determining some reservoir characteristics. *Transactions of the American Institute of Mining, Metallurgical and Petroleum Engineers*, 146, 54–62.
- Best, A., McCann, C. & Sothcott, J. (1994) The relationships between the velocities, attenuations and petrophysical properties of reservoir sedimentary rocks 1. *Geophysical Prospecting*, 42, 151–178.
- Best, A.I. (1992) *The prediction of the reservoir properties of sedimentary rocks from seismic measurements*. Doctoral dissertation, University of Reading.
- Best, A.I. & McCann, C. (1995) Seismic attenuation and pore-fluid viscosity in clay-rich reservoir sandstones. *Geophysics*, 60, 1386–1397.
- Best, A.I. & Sams, M.S. (1997) Compressional wave velocity and attenuation at ultrasonic and sonic frequencies in near-surface sedimentary rocks. *Geophysical Prospecting*, 45, 327–344.
- Biot, M.A. (1956) Theory of propagation of elastic waves in a fluid-saturated porous solid. II. Higher frequency range. *The Journal of the Acoustical Society of America*, 28, 179–191.
- Carcione, J.M., Gei, D., Picotti, S. & Michelini, A. (2012) Cross-hole electromagnetic and seismic modeling for CO₂ detection and monitoring in a saline aquifer. *Journal of Petroleum Science and Engineering*, 100, 162–172.
- Carcione, J.M., Seriani, G. & Gei, D. (2003) Acoustic and electromagnetic properties of soils saturated with salt water and NAPL. *Journal of Applied Geophysics*, 52, 177–191.
- Carrara, E., Mazzacca, A., Pece, R., Roberti, N. & Vanorio, T.J. (1999) Evaluation of porosity and saturation degree by laboratory joint measurements of velocity and resistivity: a model improvement. *Pure and Applied Geophysics*, 154, 211–255.
- Chauhan, S., Rühaak, W., Khan, F., Enzmann, F., Mielke, P., Kersten, M. & Sass, I. (2016) Processing of rock core microtomography images: using seven different machine learning algorithms. *Computers & Geosciences*, 86, 120–128.

- Chen, J. & Hoversten, G.M. (2012) Joint inversion of marine seismic AVA and CSEM data using statistical rock-physics models and Markov random fields. *Geophysics*, 77, R65–R80.
- Cilli, P. & Chapman, M. (2020) The Power-law relation between inclusion aspect ratio and porosity: implications for electrical and elastic modeling. *Journal of Geophysical Research: Solid Earth*, 125, e2019JB019187.
- Dvorkin, J., Mavko, G. & Nur, A. (1995) Squirt flow in fully saturated rocks. *Geophysics*, 60, 97–107.
- Dvorkin, J., Prasad, M., Sakai, A. & Lavoie, D. (1999) Elasticity of marine sediments: rock physics modeling. *Geophysical Research Letters*, 26, 1781–1784.
- Eberhart-Phillips, D., Han, D.-H. & Zoback, M.D. (1989) Empirical relationships among seismic velocity, effective pressure, porosity, and clay content in sandstone. *Geophysics*, 54, 82–89.
- Gal, D., Dvorkin, J. & Nur, A. (1998) A physical model for porosity reduction in sandstones. *Geophysics*, 63, 454–459.
- Gal, D., Dvorkin, J. & Nur, A. (1999) Elastic-wave velocities in sandstones with non-load-bearing clay. *Geophysical Research Letters*, 26, 939–942.
- Gao, S., Yang, Y., Liao, G., Xiong, W., Liu, H., Shen, R. et al. (2022) Experimental research on inter-fracture asynchronous injection-production cycle for a horizontal well in a tight oil reservoir. *Journal of Petroleum Science and Engineering*, 208, 109647.
- Gassmann, F. (1951) Elastic waves through a packing of spheres. *Geophysics*, 16, 673–685.
- Glover, P.W., Gómez, J.B. & Meredith, P. (2000) Fracturing in saturated rocks undergoing triaxial deformation using complex electrical conductivity measurements: experimental study. *Earth and Planetary Science Letters*, 183, 201–213.
- Hacikoylu, P., Dvorkin, J. & Mavko, G. (2006) Resistivity-velocity transforms revisited. *The Leading Edge*, 25, 1006–1009.
- Han, D.-H., Nur, A. & Morgan, D. (1986) Effects of porosity and clay content on wave velocities in sandstones. *Geophysics*, 51, 2093–2107.
- Han, T. (2010) *Joint elastic-electrical properties of reservoir sandstones*. Southampton: University of Southampton.
- Han, T., Best, A.I., Sothcott, J. & MacGregor, L.M. (2011a) Pressure effects on the joint elastic-electrical properties of reservoir sandstones. *Geophysical Prospecting*, 59, 506–517.
- Han, T., Best, A.I., Sothcott, J. & MacGregor, L.M. (2011b) Joint elastic-electrical properties of reservoir sandstones and their relationships with petrophysical parameters. *Geophysical Prospecting*, 59, 518–535.
- Han, T., Best, A.I., MacGregor, L.M., Sothcott, J. & Minshull, T.A. (2011c) Joint elastic-electrical effective medium models of reservoir sandstones. *Geophysical Prospecting*, 59, 777–786.
- Han, T., Best, A.I., Sothcott, J., North, L.J. & MacGregor, L.M. (2015) Relationships among low frequency (2 Hz) electrical resistivity, porosity, clay content and permeability in reservoir sandstones. *Journal of Applied Geophysics*, 112, 279–289.
- Hurst, A. & Nadeau, P.H. (1995) Clay microporosity in reservoir sandstones: an application of quantitative electron microscopy in petrophysical evaluation. *AAPG Bulletin*, 79, 563–573.
- Jones, S.M. (1995) Velocities and quality factors of sedimentary rocks at low and high effective pressures. *Geophysical Journal International*, 123, 774–780.
- Kaselow, A. & Shapiro, S.A. (2004) Stress sensitivity of elastic moduli and electrical resistivity in porous rocks. *Journal of Geophysics and Engineering*, 1, 1–11.
- Khaksar, A., Griffiths, C. & McCann, C. (1999) Compressional- and shear-wave velocities as a function of confining stress in dry sandstones. *Geophysical Prospecting*, 47, 487–508.
- Klimentos, T. & McCann, C. (1990) Relationships among compressional wave attenuation, porosity, clay content, and permeability in sandstones. *Geophysics*, 55, 998–1014.
- Koga, I., Aruga, M. & Yoshinaka, Y. (1958) Theory of plane elastic waves in a piezoelectric crystalline medium and determination of elastic and piezoelectric constants of quartz. *Physical Review Journals Archive*, 109, 1467.
- Lee, J., Byun, J., Kim, B. & Yoo, D.-G. (2017) Delineation of gas hydrate reservoirs in the Ulleung Basin using unsupervised multi-attribute clustering without well log data. *Journal of Natural Gas Science and Engineering*, 46, 326–337.
- Lee, M.W. (2011) *Connectivity equation and shaly-sand correction for electrical resistivity*. US Department of the Interior, US Geological Survey.
- Liu, Y., Harding, A., Abriel, W. & Strebelle, S. (2004) Multiple-point simulation integrating wells, three-dimensional seismic data, and geology. *AAPG Bulletin*, 88, 905–921.
- Lu, M., Cao, H., Sun, W., Yan, X., Yang, Z., Xu, Y. et al. (2019) Quantitative prediction of seismic rock physics of hybrid tight oil reservoirs of the Permian Lucaogou Formation, Junggar Basin, Northwest China. *Journal of Asian Earth Sciences*, 178, 216–223.
- Marion, D., Nur, A., Yin, H. & Han, D.-H. (1992) Compressional velocity and porosity in sand-clay mixtures. *Geophysics*, 57, 554–563.
- Marketos, G. & Best, A. (2010) Application of the BISQ model to clay squirt flow in reservoir sandstones. *Journal of Geophysical Research: Solid Earth*, 115.
- Marks, S.G. (1994) *Seismic wave attenuation from vertical seismic profiles*. Doctoral dissertation, University of Reading.
- Mavko, G., Mukerji, T. & Dvorkin, J. (2009) *The rock physics handbook: tools for seismic analysis of porous media*. Cambridge: Cambridge University Press. ISBN 0521861365.
- Mavko, G. & Mukerji, T. (1998) A rock physics strategy for quantifying uncertainty in common hydrocarbon indicators. *Geophysics*, 63, 1997–2008.
- McCann, C. & Sothcott, J. (1992) Laboratory measurements of the seismic properties of sedimentary rocks. *Geological Society, London, Special Publications*, 65, 285–297.
- Meglis, I., Greenfield, R., Engelder, T. & Graham, E. (1996) Pressure dependence of velocity and attenuation and its relationship to crack closure in crystalline rocks. *Journal of Geophysical Research: Solid Earth*, 101, 17523–17533.
- Murphy, W.F., Winkler, K.W. & Kleinberg, R.L. (1986) Acoustic relaxation in sedimentary rocks: dependence on grain contacts and fluid saturation. *Geophysics*, 51, 757–766.
- North, L., Best, A.I., Sothcott, J. & MacGregor, L. (2013) Laboratory determination of the full electrical resistivity tensor of heterogeneous carbonate rocks at elevated pressures. *Geophysical Prospecting*, 61, 458–470.
- Pang, M., Ba, J., Carcione, J.M., Balcewicz, M., Yue, W. & Saenger, E.H. (2022) Acoustic and electrical properties of tight rocks: a comparative study between experiment and theory. *Surveys in Geophysics*, 43, 1761–1791.
- Pang, M., Ba, J., Carcione, J.M., Saenger, E.H. & Banham, S. (2021) Elastic-electrical rock-physics template for the characterization of tight-oil reservoir rocks. *Lithosphere*, 2021.

- Peng, C., Zou, C., Lu, Z., Yu, C., Liu, A., Tang, Y. et al. (2018) Characteristics of gas hydrate reservoirs and their effect on petrophysical properties in the Muli area, Qinghai-Tibetan plateau permafrost. *Journal of Natural Gas Science and Engineering*, 57, 266–283.
- Revil, A. & Glover, P.W.J. (1998) Nature of surface electrical conductivity in natural sands, sandstones, and clays. *Geophysical Research Letters*, 25, 691–694.
- Salem, H.S. (2001) Relationships among formation resistivity factor, compressional wave velocity, and porosity for reservoirs saturated with multiphase fluids. *Energy Sources*, 23, 675–685.
- Sharp, A.J. (1995) *Seismic properties of reservoir rocks from the Morecambe Bay gas fields*. Reading: University of Reading.
- Sheng, P. & Callegari, A. (1984) Differential effective medium theory of sedimentary rocks. *Applied Physics Letters*, 44, 738–740.
- Sørensen, M.K. & Fabricius, I.L. (2015) Mud-filtrate correction of sonic logs by fluid substitution: modulus and pore-fluid coupling by pore-filling clay. PhD thesis, Technical University of Denmark, Department of Civil Engineering.
- Tan, P.-N., Steinbach M. & Kumar V. (2005) *Introduction to data mining*. Boston: Addison Wesley.
- Vernik, L. (1994) Predicting lithology and transport properties from acoustic velocities based on petrophysical classification of siliciclastics. *Geophysics*, 59, 420–427.
- Winkler, K. & Plona, T. (1982) Technique for measuring ultrasonic velocity and attenuation spectra in rocks under pressure. *Journal of Geophysical Research: Solid Earth*, 87, 10776–10780.
- Worthington, P. (1982) The influence of shale effects upon the electrical resistivity of reservoir rocks. *Geophysical Prospecting*, 30, 673–687.
- Zhang, L., Ba, J., Li, C., Carcione, J.M. & Zhou, F. (2022) Joint inversion of the unified pore geometry of tight sandstones based on elastic and electrical properties. *Journal of Petroleum Science and Engineering*, 219, 111109.

How to cite this article: Aladwani, N.S., North, L.J., Falcon-Saurez, I.H. & Best, A.I. (2023) Shale distribution effects on the joint elastic–electrical properties in reservoir sandstone. *Geophysical Prospecting*, 1–24.
<https://doi.org/10.1111/1365-2478.13331>

APPENDIX A

TABLE A1 Joint elastic–electrical properties on 12 sandstone samples in this study

Sample	50 MPa					
	V_p	Q_p	V_s	Q_s	ρ	F
S-38660 a 4369	4636	70.8	2629	60.1	44.3	208.1
S-38653 6 IVI-4134V	4607	68.5	2816	43.5	23.9	112.1
NI-38631 a NI-3615H	4587	97.6	2886	74.2	13.3	62.2
S-38606 F1-3109	3724	25.6	2227	6.7	12.1	56.6
S-38645 a NI-3942H	4830	39.2	3144	24.4	7.4	34.7
S-38656 a NI-4179	4556	39.9	2691	22.0	3.1	14.6
S-38628 a NI-3516	4608	21.3	2875	17.4	4.7	22.0
S-37400 AH86504	4099	40.0	2339	20.2	91.1	427.6
S-37402 AH8714V	3996	42.5	2329	28.2	16.7	78.6
S-37416 7575.2 H D	4673	57.5	2916	28.7	35.9	168.6
S-37404 8761V	3328	16.2	2449	15.9	5.1	23.9
S-37395 8635V	3845	34.6	2297	17.1	6.7	31.4
Sample	40 MPa					
	V_p	Q_p	V_s	Q_s	ρ	F
S-38660 a 4369	4612	65.4	2595	54.7	40.4	189.5
S-38653 6 IVI-4134V	4567	55.1	2788	38.9	22.6	105.9
NI-38631 a NI-3615H	4554	96.4	2885	72.2	12.7	59.8
S-38606 F1-3109	3695	23.6	2198	6.7	11.9	55.9
S-38645 a NI-3942H	4810	37.4	3130	24.2	7.2	33.9

(Continues)

TABLE A1 (Continued)

Sample	40 MPa					
	V_p	Q_p	V_s	Q_s	ρ	F
S-38656 a NI-4179	4536	37.9	2658	21.3	3.1	14.3
S-38628 a NI-3516	4580	19.2	2849	15.5	4.7	21.9
S-37400 AH86504	4060	37.4	2282	18.0	91.0	427.1
S-37402 AH8714V	3936	36.0	2283	26.0	16.7	78.3
S-37416 7575.2 H D	4556	51.0	2835	25.5	33.7	158.1
S-37404 8761V	3306	14.7	2432	14.4	5.1	23.7
S-37395 8635V	3819	32.2	2284	16.0	6.7	31.3
Sample	26 MPa					
	V_p	Q_p	V_s	Q_s	ρ	F
S-38660 a 4369	4541	48.5	2503	37.8	37.7	176.9
S-38653 6 IVI-4134V	4469	34.7	2711	25.3	20.2	94.6
NI-38631 a NI-3615H	4508	77.6	2834	49.2	12.0	56.5
S-38606 F1-3109	3630	18.7	2129	6.5	11.8	55.3
S-38645 a NI-3942H	4751	31.4	3084	24.1	7.2	33.9
S-38656 a NI-4179	4454	33.0	2565	16.7	3.0	14.2
S-38628 a NI-3516	4547	13.3	2805	10.7	4.5	21.2
S-37400 AH86504	3977	33.4	2225	16.3	85.6	401.9
S-37402 AH8714V	3862	29.1	2230	22.2	16.6	77.9
S-37416 7575.2 H D	4438	33.2	2753	16.6	29.4	137.9
S-37404 8761V	3270	11.1	2426	10.8	5.0	23.6
S-37395 8635V	3770	25.6	2260	12.7	6.5	30.6
Sample	20 MPa					
	V_p	Q_p	V_s	Q_s	ρ	F
S-38660 a 4369	4489	39.0	2411	28.3	33.1	155.2
S-38653 6 IVI-4134V	4387	24.7	2644	16.0	19.4	91.1
NI-38631 a NI-3615H	4466	67.2	2807	44.4	11.1	52.2
S-38606 F1-3109	3595	17.0	2081	6.4	11.7	54.8
S-38645 a NI-3942H	4708	27.7	3050	24.1	7.2	33.8
S-38656 a NI-4179	4317	31.3	2479	14.3	2.9	13.6
S-38628 a NI-3516	4423	9.9	2761	7.4	4.5	21.0
S-37400 AH86504	3919	31.4	2168	14.8	81.0	380.4
S-37402 AH8714V	3808	24.7	2169	18.5	16.5	77.6
S-37416 7575.2 H D	4375	27.4	2604	13.7	28.4	133.1
S-37404 8761V	3255	9.7	2420	9.4	4.9	23.0
S-37395 8635V	3721	18.3	2235	9.1	6.5	30.4
Sample	15 MPa					
	V_p	Q_p	V_s	Q_s	ρ	F
S-38660 a 4369	4418	30.0	2390	19.3	32.3	151.5
S-38653 6 IVI-4134V	4282	17.2	2564	9.7	16.7	78.3
NI-38631 a NI-3615H	4407	55.3	2751	31.5	9.3	43.5
S-38606 F1-3109	3569	13.7	2028	6.3	11.5	54.2
S-38645 a NI-3942H	4656	23.2	3004	22.4	7.0	33.1

(Continues)

TABLE A1 (Continued)

Sample	15 MPa						
	V_p	Q_p	V_s	Q_s	ρ	F	
S-38656 a NI-4179	4171	28.0	2381	12.0	2.8	13.1	
S-38628 a NI-3516	4333	8.1	2618	5.1	4.4	20.5	
S-37400 AH86504	3705	28.5	2112	13.6	74.6	350.3	
S-37402 AH8714V	3740	20.3	2152	15.9	16.3	76.3	
S-37416 7575.2 H D	4262	19.1	2455	9.6	24.7	116.1	
S-37404 8761V	3240	8.6	2415	8.3	4.8	22.5	
S-37395 8635V	3679	13.7	2214	6.8	6.4	29.9	
Sample	8 MPa						
	V_p	Q_p	V_s	Q_s	ρ	F	
S-38660 a 4369	4248	19.1	2384	8.4	29.9	140.5	
S-38653 6 IVI-4134V	4084	12.9	2483	6.9	15.0	70.2	
NI-38631 a NI-3615H	4277	36.3	2647	22.7	9.0	42.3	
S-38606 F1-3109	3443	9.0	1976	6.0	11.0	51.6	
S-38645 a NI-3942H	4514	17.1	2912	16.5	6.3	29.7	
S-38656 a NI-4179	3923	23.3	2254	8.1	2.6	12.1	
S-38628 a NI-3516	4216	6.3	2374	3.2	4.3	20.2	
S-37400 AH86504	3490	22.9	2055	12.6	60.0	281.9	
S-37402 AH8714V	3578	13.0	2100	11.3	16.0	75.3	
S-37416 7575.2 H D	4043	12.6	2306	6.3	20.6	96.9	
S-37404 8761V	3225	6.7	2411	6.4	4.6	21.5	
S-37395 8635V	3586	9.0	2167	4.5	6.3	29.6	
Sample	Porosity (%)		Permeability (mD)		Source		
S-38660 a 4369	10		0.025		Sharp (1995)		
S-38653 6 IVI-4134V	9		0.032		Sharp (1995)		
NI-38631 a NI-3615H	12.7		390		Sharp (1995)		
S-38606 F1-3109	21.2		650		Sharp (1995)		
S-38645 a NI-3942H	10.4		0.098		Sharp (1995)		
S-38656 a NI-4179	13.2		5.8		Sharp (1995)		
S-38628 a NI-3516	13.3		320		Sharp (1995)		
S-37400 AH86504	13.9		0.7		Marks (1994)		
S-37402 AH8714V	15.7		7		Marks (1994)		
S-37416 7575.2 H D	9.6		0.9		Marks (1994)		
S-37404 8761V	23.1		10		Marks (1994)		
S-37395 8635V	18.2		404		Marks (1994)		
ρ	Saturation bulk density						
M_{sat}	Saturated compressional modulus						
G	Shear modulus						
K_{sat}	Saturated bulk modulus						
K_{dry}	Dry bulk modulus						
M_{dry}	Dry compressional modulus						
Sample	50 MPa						
	ρ	M_{sat}	G	K_{sat}	K_{dry}	M_{dry}	Φ_{frame}
S-38660 a 4369	2.460	52.872	17.003	30.201	28.975	51.645	0.132
S-38653 6 IVI-4134V	2.500	53.061	19.825	26.628	23.418	49.850	0.138
NI-38631 a NI-3615H	2.380	50.077	19.823	23.646	20.125	46.556	0.150

(Continues)

TABLE A1 (Continued)

50 MPa							
Sample	ρ	M_{sat}	G	K_{sat}	K_{dry}	M_{dry}	Φ_{frame}
S-38606 F1-3109	2.370	32.868	11.754	17.195	12.904	28.576	0.227
S-38645 a NI-3942H	2.550	59.489	25.206	25.881	22.792	56.401	0.115
S-38656 a NI-4179	2.430	50.440	17.597	26.977	25.100	48.563	0.143
S-38628 a NI-3516	2.510	53.296	20.747	25.634	23.243	50.906	0.134
S-37400 AH86504	2.500	42.005	13.677	23.768	20.677	38.914	0.181
S-37402 AH8714V	2.340	37.365	12.693	20.442	16.191	33.115	0.206
S-37416 7575.2 H D	2.480	54.156	21.088	26.039	22.722	50.838	0.135
S-37404 8761V	2.170	24.034	13.015	6.681	3.007	14.346	0.304
S-37395 8635V	2.130	31.490	11.238	16.506	10.936	25.920	0.240
40 MPa							
Sample	ρ	M_{sat}	G	K_{sat}	K_{dry}	M_{dry}	Φ_{frame}
S-38660 a 4369	2.460	52.326	16.566	30.238	29.024	51.111	0.134
S-38653 6 IVI-4134V	2.500	52.144	19.432	26.234	22.763	48.672	0.143
NI-38631 a NI-3615H	2.380	49.359	19.809	22.946	19.027	45.440	0.155
S-38606 F1-3109	2.370	32.358	11.450	17.091	12.752	28.018	0.230
S-38645 a NI-3942H	2.550	58.997	24.982	25.688	22.487	55.797	0.117
S-38656 a NI-4179	2.430	49.998	17.168	27.107	25.278	48.169	0.144
S-38628 a NI-3516	2.510	52.651	20.373	25.487	23.033	50.197	0.137
S-37400 AH86504	2.500	41.209	13.019	23.851	20.799	38.158	0.184
S-37402 AH8714V	2.340	36.252	12.196	19.990	15.490	31.752	0.212
S-37416 7575.2 H D	2.480	51.478	19.932	24.901	20.815	47.392	0.147
S-37404 8761V	2.170	23.717	12.835	6.604	3.139	13.974	0.306
S-37395 8635V	2.130	31.066	11.111	16.250	10.530	25.345	0.243
26 MPa							
Sample	ρ	M_{sat}	G	K_{sat}	K_{dry}	M_{dry}	Φ_{frame}
S-38660 a 4369	2.460	50.727	15.412	30.178	28.943	49.492	0.140
S-38653 6 IVI-4134V	2.500	49.930	18.374	25.431	21.389	45.888	0.153
NI-38631 a NI-3615H	2.380	48.367	19.115	22.880	18.922	44.408	0.159
S-38606 F1-3109	2.370	31.229	10.742	16.906	12.482	26.805	0.236
S-38645 a NI-3942H	2.550	57.559	24.253	25.221	21.739	54.077	0.123
S-38656 a NI-4179	2.430	48.207	15.988	26.890	24.980	46.297	0.151
S-38628 a NI-3516	2.510	51.895	19.749	25.563	23.142	49.474	0.140
S-37400 AH86504	2.500	39.541	12.377	23.039	19.586	36.088	0.193
S-37402 AH8714V	2.340	34.901	11.637	19.386	14.539	30.054	0.220
S-37416 7575.2 H D	2.480	48.846	18.796	23.784	18.841	43.902	0.161
S-37404 8761V	2.170	23.204	12.771	6.175	3.879	13.149	0.311
S-37395 8635V	2.130	30.273	10.879	15.768	9.756	24.261	0.249
20 MPa							
Sample	ρ	M_{sat}	G	K_{sat}	K_{dry}	M_{dry}	Φ_{frame}
S-38660 a 4369	2.460	49.572	14.300	30.505	29.380	48.446	0.143
S-38653 6 IVI-4134V	2.500	48.114	17.477	24.812	20.290	43.592	0.162
NI-38631 a NI-3615H	2.380	47.469	18.753	22.466	18.258	43.262	0.163
S-38606 F1-3109	2.370	30.630	10.263	16.945	12.539	26.224	0.239
S-38645 a NI-3942H	2.550	56.521	23.721	24.893	21.204	52.833	0.128
S-38656 a NI-4179	2.430	45.287	14.933	25.375	22.851	42.762	0.165

(Continues)

TABLE A1 (Continued)

Sample	20 MPa						
	ρ	M_{sat}	G	K_{sat}	K_{dry}	M_{dry}	Φ_{frame}
S-38628 a NI-3516	2.510	49.103	19.134	23.591	20.238	45.750	0.154
S-37400 AH86504	2.500	38.396	11.751	22.729	19.113	34.781	0.199
S-37402 AH8714V	2.340	33.932	11.009	19.254	14.329	29.007	0.225
S-37416 7575.2 H D	2.480	47.469	16.816	25.047	21.065	43.487	0.162
S-37404 8761V	2.170	22.991	12.708	6.047	4.102	12.843	0.313
S-37395 8635V	2.130	29.492	10.640	15.305	9.005	23.191	0.254
Sample	20 MPa						
	ρ	M_{sat}	G	K_{sat}	K_{dry}	M_{dry}	Φ_{frame}
S-38660 a 4369	2.460	48.016	14.052	29.280	27.718	46.454	0.151
S-38653 6 IVI-4134V	2.500	45.839	16.435	23.925	18.653	40.566	0.174
NI-38631 a NI-3615H	2.380	46.224	18.012	22.208	17.839	41.855	0.169
S-38606 F1-3109	2.370	30.188	9.747	17.192	12.899	25.895	0.240
S-38645 a NI-3942H	2.550	55.280	23.011	24.598	20.717	51.399	0.133
S-38656 a NI-4179	2.430	42.275	13.776	23.907	20.686	39.054	0.180
S-38628 a NI-3516	2.510	47.125	17.203	24.187	21.135	44.073	0.160
S-37400 AH86504	2.500	34.318	11.151	19.449	13.827	28.696	0.227
S-37402 AH8714V	2.340	32.731	10.837	18.282	12.758	27.207	0.234
S-37416 7575.2 H D	2.480	45.048	14.947	25.119	21.188	41.117	0.172
S-37404 8761V	2.170	22.780	12.656	5.905	4.348	12.527	0.315
S-37395 8635V	2.130	28.830	10.441	14.909	8.354	22.275	0.259
Sample	8 MPa						
	ρ	M_{sat}	G	K_{sat}	K_{dry}	M_{dry}	Φ_{frame}
S-38660 a 4369	2.460	44.392	13.981	25.750	22.426	41.067	0.172
S-38653 6 IVI-4134V	2.500	41.698	15.413	21.147	12.983	33.534	0.204
NI-38631 a NI-3615H	2.380	43.537	16.676	21.302	16.340	38.574	0.182
S-38606 F1-3109	2.370	28.095	9.254	15.756	10.779	23.118	0.255
S-38645 a NI-3942H	2.550	51.959	21.623	23.128	18.192	47.024	0.149
S-38656 a NI-4179	2.430	37.398	12.346	20.937	15.975	32.436	0.209
S-38628 a NI-3516	2.510	44.614	14.146	25.753	23.412	42.274	0.167
S-37400 AH86504	2.500	30.450	10.558	16.374	8.329	22.406	0.258
S-37402 AH8714V	2.340	29.957	10.319	16.198	9.237	22.997	0.255
S-37416 7575.2 H D	2.480	40.538	13.188	22.954	17.301	34.885	0.198
S-37404 8761V	2.170	22.569	12.614	5.751	-4.617	12.202	0.317
S-37395 8635V	2.130	27.391	10.002	14.054	6.931	20.267	0.270

APPENDIX B

TABLE B1 Regression coefficient in Equations (3)–(9) for the elastic electrical properties of the 12 sandstone samples

Sample	V_p			$1/Q_p$		
	A	B	C	A	B	C
S-38660 a 4369	4649.914	730.150	0.075	0.014	−0.084	0.096
S-38653 6 IVI-4134V	4641.606	937.033	0.065	0.009	−0.115	0.062
NI-38631 a NI-3615H	4593.553	568.407	0.074	0.010	−0.041	0.107
S-38606 F1-3109	3741.022	470.275	0.060	0.040	−0.165	0.104
S-38645 a NI-3942H	4839.974	591.609	0.075	0.025	−0.069	0.088
S-38656 a NI-4179	4595.293	1252.970	0.076	0.024	−0.032	0.068
S-38628 a NI-3516	4557.799	199.999	0.100	0.031	−0.199	0.054
S-37400 AH86504	4646.538	729.224	0.063	0.025	−0.035	0.080
S-37402 AH8714V	4018.481	697.953	0.059	0.024	−0.113	0.097
S-37416 7575.2 H D	4732.702	1006.187	0.049	0.015	−0.126	0.085
S-37404 8761V	3401.619	212.461	0.020	0.051	−0.150	0.053
S-37395 8635V	3870.585	444.766	0.056	0.026	−0.182	0.093
Sample	V_s			$1/Q_s$		
	A	B	C	A	B	C
S-38660 a 4369	2830.986	565.989	0.020	0.018	−0.337	0.150
S-38653 6 IVI-4134V	2889.750	584.265	0.043	0.015	−0.249	0.078
NI-38631 a NI-3615H	2899.554	474.929	0.079	0.012	−0.062	0.080
S-38606 F1-3109	2274.419	424.225	0.040	0.012	−0.154	0.003
S-38645 a NI-3942H	3159.452	422.410	0.067	0.041	−0.139	0.246
S-38656 a NI-4179	2756.856	763.591	0.051	0.044	−0.170	0.095
S-38628 a NI-3516	2875.893	1203.006	0.108	0.050	−0.569	0.094
S-37400 AH86504	2428.051	492.592	0.032	0.036	−0.055	0.027
S-37402 AH8714V	2421.958	406.438	0.027	0.035	−0.109	0.088
S-37416 7575.2 H D	3007.689	1055.343	0.048	0.031	−0.252	0.085
S-37404 8761V	2489.808	90.667	0.014	0.052	−0.159	0.054
S-37395 8635V	2309.207	222.383	0.056	0.053	−0.363	0.094
Sample	Q_p			Q_s		
	A	B	C	A	B	C
S-38660 a 4369	101.246	101.319	0.025	90.531	101.321	0.025
S-38653 6 IVI-4134V	619.358	621.644	0.002	143.886	148.377	0.008
NI-38631 a NI-3615H	110.287	108.112	0.046	111.929	108.634	0.023
S-38606 F1-3109	30.158	28.259	0.036	7.135	1.273	0.024
S-38645 a NI-3942H	44.410	38.375	0.041	24.379	41.047	0.207
S-38656 a NI-4179	44.484	28.258	0.036	26.431	24.699	0.036
S-38628 a NI-3516	76.892	74.838	0.006	36.738	38.127	0.014
S-37400 AH86504	42.830	27.822	0.043	31.964	21.564	0.012
S-37402 AH8714V	60.198	55.991	0.022	32.871	29.065	0.037

(Continues)

TABLE B1 (Continued)

Sample	Q_p			Q_s		
	A	B	C	A	B	C
S-37416 7575.2 H D	152.183	151.857	0.010	108.347	107.516	0.006
S-37404 8761V	34.607	30.373	0.010	37.866	33.809	0.009
S-37395 8635V	46.759	48.880	0.029	22.899	23.973	0.030
Sample	ρ					
	A	B	C			
S-38660 a 4369		86.587	60.176	0.007		
S-38653 6 IVI-4134V		57.734	44.091	0.006		
NI-38631 a NI-3615H		14.425	7.829	0.039		
S-38606 F1-3109		12.105	1.171	0.043		
S-38645 a NI-3942H		7.300	4.215	0.183		
S-38656 a NI-4179		3.114	1.034	0.081		
S-38628 a NI-3516		4.776	0.668	0.039		
S-37400 AH86504		92.392	65.089	0.087		
S-37402 AH8714V		16.475	0.007	0.039		
S-37416 7575.2 H D		39.897	25.676	0.036		
S-37404 8761V		5.115	1.030	0.080		
S-37395 8635V		6.822	0.703	0.034		
Sample	V_p – Apparent formation factor			R^2	Adjusted R^2	
	A	B				
S-38660 a 4369	0.0010	0.779		0.864	0.830	
S-38653 6 IVI-4134V	0.0009	0.540		0.978	0.973	
NI-38631 a NI-3615H	0.0014	-2.179		0.919	0.899	
S-38606 F1-3109	0.0003	2.853		0.971	0.964	
S-38645 a NI-3942H	0.0005	1.355		0.875	0.844	
S-38656 a NI-4179	0.0003	1.385		0.993	0.992	
S-38628 a NI-3516	0.0002	2.110		0.931	0.913	
S-37400 AH86504	0.0007	3.341		0.974	0.967	
S-37402 AH8714V	0.0001	3.939		0.952	0.940	
S-37416 7575.2 H D	0.0009	0.891		0.991	0.988	
S-37404 8761V	0.0009	0.132		0.792	0.739	
S-37395 8635V	0.0002	2.520		0.960	0.950	